Monthly Notices of the ROYAL ASTRONOMICAL SOCIETY

MNRAS **441,** 1017–1039 (2014) doi:10.1093/mnras/stu510

Herschel★-ATLAS: properties of dusty massive galaxies at low and high redshifts

K. Rowlands,[1,2]† L. Dunne,[3] S. Dye,[1] A. Aragón-Salamanca,[1] S. Maddox,[3] E. da Cunha,[4] D. J. B. Smith,[5] N. Bourne,[1,6] S. Eales,[7] H. L. Gomez,[7] I. Smail,[8] M. Alpaslan,[9,2] C. J. R. Clark,[7] S. Driver,[9,2] E. Ibar,[10] R. J. Ivison,[11,6] A. Robotham,[9,2] M. W. L. Smith[7] and E. Valiante[7]

[1]*School of Physics and Astronomy, The University of Nottingham, University Park Campus, Nottingham NG7 2RD, UK*
[2]*(SUPA) School of Physics and Astronomy, University of St Andrews, North Haugh, St Andrews, Fife KY16 9SS, UK*
[3]*Department of Physics and Astronomy, University of Canterbury, Private Bag 4800, Christchurch, New Zealand*
[4]*Max Planck Institute for Astronomy, Konigstuhl 17, D-69117, Heidelberg, Germany*
[5]*Centre for Astrophysics, Science and Technology Research Institute, University of Hertfordshire, Hatfield, Herts AL10 9AB, UK*
[6]*Institute for Astronomy, The University of Edinburgh, Royal Observatory, Blackford Hill, Edinburgh EH9 3HJ, UK*
[7]*School of Physics and Astronomy, Cardiff University, Queens Buildings, The Parade, Cardiff CF24 3AA, UK*
[8]*Institute for Computational Cosmology, Department of Physics, Durham University, South Road, Durham DH1 3LE, UK*
[9]*International Centre for Radio Astronomy (ICRAR), University of Western Australia, Crawley, WA 6009, Australia*
[10]*Instituto de Física y Astronomía, Universidad de Valparaíso, Avda. Gran Bretaña 1111, Playa Ancha, Valparaíso 2360102, Chile*
[11]*European Southern Observatory, Karl Schwarzschild Strasse 2, D-85748 Garching, Germany*

Accepted 2014 March 9. Received 2014 March 5; in original form 2014 January 10

ABSTRACT

We present a comparison of the physical properties of a rest-frame 250-μm-selected sample of massive, dusty galaxies from $0 < z < 5.3$. Our sample comprises 29 high-redshift submillimetre galaxies (SMGs) from the literature and 843 dusty galaxies at $z < 0.5$ from the *Herschel*-Astrophysical TeraHertz Large Area Survey (H-ATLAS), selected to have a similar stellar mass to the SMGs. The $z > 1$ SMGs have an average star formation rate (SFR) of 390^{+80}_{-70} $\mathrm{M_\odot\ yr^{-1}}$, which is 120 times that of the low-redshift sample matched in stellar mass to the SMGs ($\mathrm{SFR} = 3.3 \pm 0.2\ \mathrm{M_\odot\ yr^{-1}}$). The SMGs harbour a substantial mass of dust ($1.2^{+0.3}_{-0.2} \times 10^9$ $\mathrm{M_\odot}$), compared to $(1.6 \pm 0.1) \times 10^8$ $\mathrm{M_\odot}$ for low-redshift dusty galaxies. At low redshifts, the dust luminosity is dominated by the diffuse interstellar medium, whereas a large fraction of the dust luminosity in SMGs originates from star-forming regions. At the same dust mass, SMGs are offset towards a higher SFR compared to the low-redshift H-ATLAS galaxies. This is not only due to the higher gas fraction in SMGs but also because they are undergoing a more efficient mode of star formation, which is consistent with their bursty star formation histories. The offset in SFR between SMGs and low-redshift galaxies is similar to that found in CO studies, suggesting that dust mass is as good a tracer of molecular gas as CO.

Key words: dust, extinction – galaxies: evolution – galaxies: fundamental parameters – galaxies: high-redshift – galaxies: ISM – submillimetre: galaxies.

1 INTRODUCTION

The first blind submillimetre surveys discovered a population of luminous ($L_{\mathrm{IR}} > 10^{12}\ \mathrm{L_\odot}$), highly star-forming (100–1000 $\mathrm{M_\odot\ yr^{-1}}$), dusty ($10^{8-9}$ $\mathrm{M_\odot}$) galaxies at high redshift (Smail, Ivison & Blain 1997; Barger et al. 1998; Hughes et al. 1998; Eales et al. 1999). These submillimetre galaxies (SMGs) are thought to be undergoing intense, obscured starbursts (Alexander et al. 2005; Greve et al. 2005; Tacconi et al. 2006; Pope et al. 2008), which may be driven by gas-rich major mergers (e.g. Tacconi et al. 2008; Engel et al. 2010; Riechers et al. 2011; Wang et al. 2011; Bothwell et al. 2013), or streams of cold gas (Dekel et al. 2009; Davé et al. 2010; van de Voort et al. 2011). Measurements of the stellar masses, star formation histories (SFHs) and clustering properties of SMGs indicate that they may be the progenitors of massive elliptical galaxies observed in the local Universe (Eales et al. 1999; Blain et al. 2002; Dunne, Eales & Edmunds 2003; Chapman et al. 2005;

★*Herschel* is an ESA Space Observatory with science instruments provided by European-led Principal Investigator consortia and with important participation from NASA.

†E-mail: ker7@st-andrews.ac.uk

© 2014 The Authors
Published by Oxford University Press on behalf of the Royal Astronomical Society

Swinbank et al. 2006; Hainline et al. 2011; Hickox et al. 2012). Due to their extreme far-infrared (FIR) luminosities, it was proposed that SMGs were the high-redshift analogues of local ultra-luminous infrared galaxies (ULIRGs), which are undergoing major mergers. Recent observations (Magnelli et al. 2012a; Targett et al. 2013) and simulations (Davé et al. 2010; Hayward et al. 2011) have suggested that the SMG population is a mix of starbursts and massive star-forming galaxies, with the most luminous SMGs ($L_{\rm IR} \sim 10^{13}$ L$_\odot$) being major mergers and lower luminosity SMGs being consistent with turbulent, star-forming discs. There are, however, still considerable uncertainties in the physical properties of SMGs (e.g. Hainline et al. 2011; Michałowski et al. 2012b), which affects our view of how SMGs fit into the general picture of galaxy evolution.

SMGs are found to typically reside at $z \sim 1$–3 (Chapman et al. 2005; Chapin et al. 2009; Lapi et al. 2011; Wardlow et al. 2011; Michałowski et al. 2012a; Yun et al. 2012; Simpson et al. 2014), partly due to the effect of the negative *k*-correction, which allows galaxies which are bright at >850 μm to be detected across a large range in redshift (Blain et al. 2002). Due to the long integration times required to survey a large area of sky at 850 μm, submillimetre survey volumes at low redshift have until recently been relatively small, leading to difficulties in obtaining a representative sample of dusty galaxies at low redshift. With the launch of the *Herschel Space Observatory* (Pilbratt et al. 2010), we can now get an unprecedented view of dust in local galaxies. *Herschel* observed at FIR–submillimetre wavelengths across and beyond the peak of the dust emission, making it an unbiased tracer of the dust mass in galaxies. The *Herschel* Astrophysical TeraHertz Large Area Survey (H-ATLAS; Eales et al. 2010a) is the largest area extragalactic survey carried out with *Herschel* and has allowed us to quantify the amount of dust in galaxies at low redshift. By studying galaxies selected at 250 μm, Smith et al. (2012b) found an average dust mass of 9.1×10^7 M$_\odot$ in local ($z < 0.35$) dusty galaxies. Furthermore, the dust mass in galaxies is found to increase by a factor of 3−4 between $0 < z < 0.3$ (Dunne et al. 2011; Bourne et al. 2012), which may be linked to higher gas fractions in galaxies at earlier epochs (Geach et al. 2011; Combes et al. 2013; Tacconi et al. 2013).

The question of how the modes of star formation in SMGs relates to those in local star-forming galaxies warrants a comparison between galaxy samples. Comparisons between SMGs and the low-redshift galaxy population has been carried out for small galaxy samples, e.g. Santini et al. (2010) compared the properties of 21 SMGs to 26 local spirals from SINGS (Kennicutt et al. 2003) and 24 local ULIRGs from Clements, Dunne & Eales (2010) and found that SMGs have dust-to-stellar mass ratios 30 times larger than local spirals, and a factor of 6 more than local ULIRGs. However, a comparison to large representative samples of the general dusty galaxy population has not yet been carried out. In this paper, we investigate the physical properties of dusty galaxies over a wide range in cosmic time, utilizing carefully selected samples of high- and low-redshift galaxies which occupy comparable comoving volumes of $\sim 10^8$ Mpc^3.

We describe our sample selection in Section 2 and spectral energy distribution (SED) fitting method to explore the properties of SMGs in Section 3. Our results are presented in Section 4 and our conclusions are in Section 5. We adopt a cosmology with $\Omega_{\rm m} = 0.27$, $\Omega_\Lambda = 0.73$ and $H_0 = 71$ km s^{-1} Mpc^{-1}.

2 SAMPLE SELECTION

In order to investigate the physical properties of dusty galaxies over a range of redshifts, we construct a sample selected at ~ 250 μm rest-frame wavelength. This comprises panchromatic photometry of low-redshift galaxies from the H-ATLAS Phase 1 catalogue, and a sample of high-redshift SMGs presented in Magnelli et al. (2012a).

2.1 Low-redshift H-ATLAS sample

The H-ATLAS is an ∼590 deg^2 survey undertaken by *Herschel* at 100, 160, 250, 350 and 500 μm to provide an unbiased view of the submillimetre Universe. Observations were carried out in parallel mode using the PACS (Poglitsch et al. 2010) and SPIRE (Griffin et al. 2010) instruments simultaneously. The observations in the Phase 1 field cover an area of ∼161 deg^2 centred on the Galaxy And Mass Assembly (GAMA) 9, 12 and 15 hr equatorial fields (Driver et al. 2011). Details of the map making can be found in Pascale et al. (2011), Ibar et al. (2010) and Smith et al. (in preparation). We use the catalogue of $\geq 5\sigma$ detections in the 250 μm band (Rigby et al. 2011; Valiante et al., in preparation) produced using the MAD-X algorithm (Maddox et al., in preparation). Fluxes at 350 and 500 μm are measured at the location of the 250-μm-fitted position. A likelihood-ratio analysis (Sutherland & Saunders 1992; Smith et al. 2011) was then performed to match the 250 μm sources to the Sloan Digital Sky Survey (SDSS) DR7 (Abazajian et al. 2009) galaxies with $r < 22.4$. This method accounts for the possibility that the true counterpart is below the optical magnitude limit and uses the positional uncertainty as well as empirical magnitude priors to estimate the probability (reliability) of a submillimetre source being the true association of a given optical counterpart. SDSS sources with reliability $R \geq 0.8$ are considered to be likely matches to submillimetre sources.

PACS 100 and 160 μm flux densities were measured for all 250 μm sources[1] by placing apertures at the SPIRE positions. Aperture photometry for extended SPIRE sources was also performed according to the procedure described in Rigby et al. (2011). The final catalogue has 103 721 sources detected at 250 μm at $\geq 5\sigma$, with flux estimates in each of the other four bands at that position. The 5σ noise levels were 130, 130, 30, 37 and 41 mJy per beam at 100, 160, 250, 350 and 500 μm, respectively; with beam sizes of 9, 13, 18, 25 and 35 arcsec in these bands.

From this catalogue, there are 29 787 reliable optical counterparts to H-ATLAS sources; with 14 920 sources having good quality spectroscopic redshifts and 14 867 sources having photometric redshifts. The contamination rate by false identifications is given by $\sum(1 - R)$ following Smith et al. (2011), and is expected to be 3.8 per cent. The median and 84th–16th percentile range of 250 μm flux densities of sources with reliable counterparts with good quality spectroscopic redshifts at $z < 0.5$ is $0.05^{+0.04}_{-0.01}$ Jy. Around two-thirds of the sources without reliable optical counterparts are unidentified because their counterparts lie below the optical magnitude limit, and these sources mostly reside at $z > 0.5$ (see Dunne et al. 2011). The remaining unidentified sources are believed to have a counterpart in the SDSS catalogue but we are unable to unambiguously identify the correct counterpart in these cases due to near neighbours and the non-negligible probability of a background galaxy of the same magnitude being found at this distance. The optically identified sources are believed to be a representative sample of all H-ATLAS sources at $z \leq 0.35$ (Smith et al. 2012b).

[1] Except those with SDSS *r*-band isophotal major axis (isoA) >30 arcsec, where reliable PACS fluxes cannot be obtained due to aggressive high-pass filtering in the maps. This issue will be rectified in the public data release.

The optically identified counterparts were combined with GAMA data (Baldry et al. 2010; Robotham et al. 2010; Driver et al. 2011) to provide *r*-band defined matched aperture photometry as described in Hill et al. (2011). The FUV and NUV photometry is from *GALEX* (Martin et al. 2005; Morrissey et al. 2007, Seibert et al., in preparation), and is a reconstruction of the true UV flux of a given GAMA object. This accounts for cases where multiple GAMA and *GALEX* objects are associated with each other. Optical *ugriz* magnitudes are derived from SDSS DR6 imaging (Adelman-McCarthy et al. 2008) and near-infrared (NIR) *YJHK* photometry are from UKIDSS-LAS imaging (Lawrence et al. 2007). All UV–NIR photometry has been galactic extinction corrected. Spectroscopic redshifts are included from the GAMA, SDSS and 6df Galaxy Survey catalogues for 14 490 sources at $z < 0.5$; where spectroscopic redshifts are not available, we use ANNz (Collister & Lahav 2004) neural network photometric redshifts from Smith et al. (2011). Smith et al. (2011) estimate the completeness of the H-ATLAS sample as a function of redshift by calculating the total number sources that we would expect to have a counterpart above the SDSS magnitude limit in H-ATLAS; we refer the reader to Smith et al. (2011) and Dunne et al. (2011) for further details.

2.2 High-redshift SMG sample

Estimates from submillimetre photometric redshift studies suggest that ∼50 per cent of H-ATLAS sources are at $z > 1$ (Lapi et al. 2011; Pearson et al. 2013); however, identifications to these submillimetre sources are not currently available due to the relatively shallow ancillary multiwavelength data. We therefore rely on publicly available measurements of high-redshift submillimetre galaxies (SMGs) with robust optical counterparts and spectroscopic redshifts in the literature. We utilize the compilation of SMGs in Magnelli et al. (2012a, hereafter M12) taken from blank-field (sub)millimetre surveys (850-1200 μm) which have robust counterparts identified with deep radio, interferometric submillimetre and/or mid-infrared (MIR) imaging from Chapman et al. (2005), Pope et al. (2006, 2008), Bertoldi et al. (2007), Ivison et al. (2007), Younger et al. (2007, 2009), Chapin et al. (2009), Coppin et al. (2010), Biggs et al. (2011) and Aravena et al. (in preparation). The spectroscopic redshifts in the M12 sample are from Borys et al. (2004), Chapman et al. (2005), Pope et al. (2008), Daddi et al. (2009), Coppin et al. (2010), Danielson et al. (in preparation) and Capak et al. (in preparation). The SMGs are located in fields which have excellent multiwavelength coverage [the Great Observatories Origins Deep Survey-North (GOODS-N), Extended Chandra Deep Field South (ECDFS), the Cosmological Evolution Survey (COSMOS) and Lockman Hole], which is required in order to derive statistical constraints on galaxy physical properties using SED fitting. Most crucially, all of the galaxies in our sample have well-sampled coverage of the peak of the dust emission in the FIR, which allows us to derive robust constraints on the dust luminosity of our SMGs. This coverage of the dust peak is not available for all sources in larger samples of SMGs (e.g. those from Chapman et al. 2005). Estimates of the dust luminosity and temperature are therefore often subject to assumptions about the SED shape with constraints based on only one or two FIR–submillimetre measurements.

In M12, the radio or MIPS counterparts to the SMGs were matched within 3 arcsec to *Spitzer* Multiband Imaging Photometer (MIPS; Rieke et al. 2004) 24 μm positions associated with PACS and SPIRE data at 70, 100, 160, 250, 350 and 500 μm from the PACS Evolutionary Probe (Lutz et al. 2011) and *Herschel* Multi-tiered Extragalactic Survey (HerMES; Oliver et al. 2012). The reduction of the HerMES maps is described in Smith et al. (2012a), and cross-identifications of 24 μm and SPIRE sources were performed in Roseboom et al. (2010). The PACS and SPIRE fluxes of the sources were extracted by fitting a point spread function (PSF) at the 24 μm position, which allows the flux of blended FIR sources to be recovered. Additionally, the inherent association of a SPIRE source with a more accurate 24 μm position allows for relatively easy identification of multiwavelength counterparts.

M12 present photometry for 61 galaxies; however, we only consider the 46 SMGs which are unlensed. This is because M12 found difficulty in obtaining good quality optical–NIR photometry which is required for deriving constraints on stellar masses and star formation rates (SFRs). We also conservatively exclude 6/46 sources listed in M12 which have multiple robust counterparts to the submillimetre source where both counterparts are at the same redshift. These systems are thought to be interacting, so the submillimetre emission is thought to originate from both sources and there is no way to quantify the individual contribution of each counterpart to the submillimetre emission. We note that other sources in our sample with single robust counterparts may also be interacting systems; this is discussed in Section 2.2.1. Four sources (LESS10, LOCK850.03, LOCK850.04 and LOCK850.15) have multiple robust counterparts for which only one counterpart has a spectroscopic redshift. Following M12 we include these galaxies in our sample, as the 24 μm and radio flux densities of the spectroscopic counterpart agree with the infrared luminosity computed from the FIR–submillimetre flux densities. This supports the assumption that the submillimetre emission originates from one counterpart. The inclusion or exclusion of these galaxies does not change our results. We include four galaxies which have a $<3\sigma$ detection above the confusion limit in at least one of the SPIRE bands so we do not bias our sample towards sources with warm dust temperatures. M12 note that one of these (GN15) is isolated and so its measured flux densities should be reliable; however, for the other three (GN5, GN20, GN20.2) the FIR emission is confused with that from near neighbours, which may lead to some overestimation of their FIR fluxes. For GN20, we use the *Herschel* photometry from Magdis et al. (2011), which has been carefully deblended based on 24 μm and radio positional priors. We use different symbols for these confused sources in later figures so that any systematic biases relative to the rest of the sample can be easily seen.

We match the counterpart positions presented in M12 to ancillary optical–MIR data using a 1 arcsec search radius for optical data[2] and a 2 arcsec search radius for *Spitzer* Infrared Array Camera (IRAC; Fazio et al. 2004) data. We only include a galaxy counterpart in our sample if it has IRAC data, as we expect 24-μm-detected galaxies to also have IRAC data. Across all fields we find that six sources which were included in M12 do not have optical matches within 1 arcsec. In the COSMOS field, we use the broad, medium and narrow-band photometry as presented in Ilbert et al. (2009) and Salvato et al. (2009). The public *Spitzer* IRAC photometry was retrieved from the COSMOS archive.[3] The GOODS-N multiwavelength catalogue is briefly described in Berta et al. (2010, 2011) and includes PSF-matched photometry from *HST* ACS *bviz* (version 1.0), FLAMINGOS *JHK*[4] and IRAC 3.6, 4.5, 5.8, 8.0 μm obtained with the CONVPHOT code (Grazian et al. 2006),

[2] 1 arcsec corresponds to 8.5 kpc at $z = 2$ for our adopted cosmology.
[3] http://irsa.ipac.caltech.edu/data/COSMOS/
[4] The KPNO 4 m FLAMINGOS data were kindly provided by Mark Dickinson, Kyoungsoo Lee and the GOODS team.

spectroscopic redshifts from Barger, Cowie & Wang (2008) and associated *GALEX U*-band, radio and X-ray fluxes. Deep CFHT WirCAM K_s-band photometry was taken from Wang et al. (2010) and 24 and 70 μm MIPS data are from Magnelli et al. (2011). In ECDFS, we use the compilation of photometry for SMGs presented in Wardlow et al. (2011) from the MUSYC (Gawiser et al. 2006; Taylor et al. 2009), IRAC photometry from SIMPLE (Damen et al. 2011) and GOODS/VIMOS *U*-band data from Nonino et al. (2009). In the Lockman Hole, we use the photometry described in Fotopoulou et al. (2012), which comprises UV data from *GALEX* Large Binocular Telescope (U, B, V, Y, z') and Subaru (R_c, I_c, z') photometry, J and K photometry from the UKIRT and MIR data from IRAC. We follow the recommendations in each catalogue and apply the relevant offsets to correct all of the photometry to total magnitudes. Additionally, we have removed any spurious or problematic photometry, in particular, COSMOS medium-band photometry where we suspect that strong nebular emission lines contribute significantly to the flux. Deboosted millimetre photometry is provided for some sources in M12 where available from Greve et al. (2004, 2008), Bertoldi et al. (2007), Perera et al. (2008), Scott et al. (2008, 2010), Chapin et al. (2009) and Austermann et al. (2010). The final sample comprises 34 SMGs with robust counterparts and panchromatic data from the rest-frame UV to the submillimetre.[5]

In order to account for additional uncertainties, for example, in deriving total flux measurements and photometric calibration for the wide array of multiwavelength data, we add in quadrature a calibration error to the catalogue photometric errors. For optical, NIR, MIR and FIR bands, we add in quadrature 20 per cent of the flux. We add 30 per cent of the flux for (sub)millimetre ($\geq$ 850 μm) data to account for calibration errors, the uncertainty in deboosting the fluxes and source blending. For sources which are not detected, we set the fluxes to upper limits as detailed in the respective catalogues; these are typically 5σ upper limits in the optical–NIR bands and 3σ upper limits longwards of 24 μm.

2.2.1 SMG multiplicity

Another source of uncertainty in our SMG sample is source multiplicity. Using ALMA data, Hodge et al. (2013) estimated that 35–50 per cent of single dish-detected SMGs are comprised of multiple sources. The fraction of SMGs which are multiple is likely to be slightly lower in our sample, as we have removed SMGs which have more than one robust counterpart at the same redshift. The seven SMGs in ECDFS observed by Hodge et al. (2013) confirm that 4/7 SMGs are single sources (LESS10, LESS11, LESS17, LESS18), with the ALMA position in good agreement with the radio position given in M12. One source (LESS40) was not detected above the 3σ limit; this may be due to the relatively low-quality image of this source, although it is possible that this source is comprised of multiple faint submillimetre sources which are below the ALMA detection threshold. The other two sources (LESS67 and LESS79) are comprised of multiple submillimetre counterparts, with only one component coincident with the position of the robust radio/MIPS counterpart identified in Biggs et al. (2011). Since the FIR photometry for the multicounterpart SMGs are blended, it is possible that the dust masses are overestimated. The flux for the ALMA component coincident with the LABOCA robust counterpart position amounts to 0.73 and 0.25 of the total ALMA flux in these two blended cases. Given that the flux of the ALMA counterparts are 0.87 and 0.43 of the deboosted LABOCA flux for LESS67 and LESS79, respectively, we may expect that the dust masses would be overestimated by similar factors. The change in dust mass for LESS67 is within the 1σ uncertainty on the dust masses from the SED fitting, and the change in dust mass for LESS79 is within the 3σ uncertainty on the dust mass. We find that the dust masses for these blended sources using the LABOCA fluxes are not outliers in our sample of SMGs, and are similar to the dust masses of SMGs confirmed to have a single counterpart; therefore, blending does not affect our conclusions.

3 SED FITTING

The wealth of multiwavelength coverage for our sample of dusty galaxies allows us to derive physical properties using SED fitting techniques. Due to a lack of FIR data, studies of SMGs have often derived dust luminosities and SFRs based upon fitting SEDs to 850 μm photometry alone. The availability of *Herschel* data across the peak of the dust emission provides better constraints on the dust luminosity than previous studies (e.g. Chapman et al. 2005); see M12 for a review.

We use a modified version of the physically motivated method of da Cunha, Charlot & Elbaz (2008, hereafter DCE08[6]) to recover the physical properties of the galaxies in our sample. In this method, the UV–optical radiation emitted by stellar populations is absorbed by dust, and this absorbed energy is matched to that reradiated in the FIR. Spectral libraries of 50 000 optical models, with stochastic SFHs, and 50 000 infrared models are produced at the redshift of each galaxy in our sample, containing model parameters and synthetic photometry from the UV to the millimetre. The model libraries are constructed from parameters which have prior distributions designed to reproduce the range of properties found in galaxies. The optical libraries are produced using the spectral evolution of stellar populations calculated from the latest version of the population synthesis code of Bruzual & Charlot (2003). The stellar population models include a revised prescription for thermally pulsing asymptotic giant branch (TP-AGB) stars from Marigo & Girardi (2007). A Chabrier (2003) Galactic-disc initial mass function (IMF) is assumed. The libraries contain model spectra with a wide range of SFHs, metallicities and dust attenuations. The two-component dust model of Charlot & Fall (2000) is used to calculate the attenuation of starlight by dust, which accounts for the increased attenuation of stars in birth clouds compared to old stars in the ambient interstellar medium (ISM). The model assumes angle-averaged spectral properties and so does not include any spatial or dynamical information. Hayward & Smith (in preparation) find that physical properties derived using MAGPHYS are robust to projection effects associated with different viewing angles.

The infrared libraries contain SEDs comprised of four different temperature dust components, from which the dust mass ($M_{\rm d}$) is calculated. In stellar birth clouds, these components are polycyclic aromatic hydrocarbons, hot dust (stochastically heated small grains with a temperature 130−250 K) and warm dust in thermal equilibrium (30−60 K). In the diffuse ISM, the relative fractions of these three dust components are fixed, but an additional cold dust component with an adjustable temperature between 15 and 25 K is added.

[5] The photometry for the SMGs is available electronically from VizieR: http://cdsweb.u-strasbg.fr/cgi-bin/qcat?J/MNRAS/.

[6] The DCE08 models are publicly available as a user-friendly model package MAGPHYS at www.iap.fr/magphys/.

The dust mass absorption coefficient $\kappa_\lambda \propto \lambda^{-\beta}$ has a normalization of $\kappa_{850} = 0.077\,\mathrm{m^2\,kg^{-1}}$ (Dunne et al. 2000). A dust emissivity index of $\beta = 1.5$ is assumed for warm dust and $\beta = 2.0$ for cold dust, following studies which support a value of β dependent on the temperature of the dust components (Dale & Helou 2002; Smith et al. 2012c; Davies et al. 2013), see also the review in Dunne & Eales (2001). The prior distributions for the temperature of warm dust in birth clouds ($T_{\mathrm{W}}^{\mathrm{BC}}$) and the temperature of cold dust in the diffuse ISM ($T_{\mathrm{C}}^{\mathrm{ISM}}$) are flat (see Fig. A1), so that all temperatures within the bounds of the prior have equal probability in the model libraries.

The attenuated stellar emission and dust emission models in the two spectral libraries are combined using a simple energy balance argument that the energy absorbed by dust in stellar birth clouds and the diffuse ISM is re-emitted in the FIR. In practise, this means that each model in the optical library is matched to models in the infrared library which have the same fraction of total dust luminosity contributed by the diffuse ISM (f_μ), within a tolerance of 0.15, and are scaled to the total dust luminosity[7] L_{d}. Statistical constraints on the various parameters of the model are derived using the Bayesian approach described in DCE08. Each observed galaxy SED is compared to a library of stochastic models which encompasses all plausible parameter combinations. For each galaxy, the marginalized likelihood distribution of any physical parameter is built by evaluating how well each model in the library can account for the observed properties of the galaxy (by computing the χ^2 goodness of fit). This method ensures that possible degeneracies between model parameters are included in the final probability density function (PDF) of each parameter. The effects of individual wavebands on the derived parameters are explored in DCE08 and Smith et al. (2012b), but we emphasize the importance of using the *Herschel* FIR–submillimetre data to sample the peak of the dust emission and the Rayleigh–Jeans slope in order to get reliable constraints on the dust mass and luminosity (Smith et al. 2013).

The MAGPHYS code is modified from the public version to take into account flux density upper limits in the χ^2 calculation to give additional constraints on physical parameters. If the flux upper limit is above the model SED, the upper limit does not contribute to the χ^2 value. When the model SED violates the flux upper limit, the flux upper limit is treated like all the other detected photometry by including the upper limit as a flux density (with associated photometric error) in the χ^2 calculation. Additionally, we modify the priors to take into account areas of parameter space which are not explored with the standard MAGPHYS libraries. This is important when studying a wide variety of galaxies from quiescent systems to highly obscured starburst galaxies. Section 3.1 and Appendix A outline the standard priors which are more applicable to low-redshift galaxies, and also describes the modified priors which better suit the high-redshift SMGs.

An example best-fitting SED and a set of PDFs are shown in Fig. 1. The parameters of interest are f_μ, the fraction of total dust luminosity contributed by the diffuse ISM; $M_*/\mathrm{M}_\odot$, stellar mass; $M_{\mathrm{d}}/\mathrm{M}_\odot$, dust mass; M_{d}/M_* , dust-to-stellar mass ratio; $L_{\mathrm{d}}/\mathrm{L}_\odot$, dust luminosity; $\hat{\tau}_V$, total effective V-band optical depth seen by stars in birth clouds; $\hat{\tau}_V^{\mathrm{ISM}}$, the effective V-band optical depth in the ambient ISM; $\psi/\mathrm{M}_\odot\ \mathrm{yr}^{-1}$, the SFR; and $\psi_{\mathrm{S}}/\mathrm{yr}^{-1}$, specific SFR (SSFR). For more details of the method, we refer the reader to DCE08.

[7] Integrated between 3 and 1000 μm.

3.1 Model priors

The 'standard' priors which are appropriate for low-redshift galaxies are described in detail in DCE08 and were also used in Smith et al. (2012b) to derive the properties of low-redshift H-ATLAS galaxies similar to those in this work. Initial tests with the standard priors showed that there were very few models which had a high enough SSFR to provide a good fit to the photometry of all of the high-redshift SMGs. We created modified priors to accommodate a wider range of galaxy characteristics, allowing for higher dust attenuation and SSFR than observed in most low-redshift galaxies. It is not clear whether all SMGs are similar to local ULIRGs with an obscured central starburst, as many show evidence for more extended star formation (e.g. Tacconi et al. 2008; Hainline et al. 2009; Swinbank et al. 2011; Targett et al. 2013). Our modified priors (henceforth called 'SMG priors') are a hybrid between the ULIRG priors described in da Cunha et al. (2010b) and the standard model libraries. A summary of the differences in the prior distributions and how the choice of priors affects our results is given in Appendix A.

4 PHYSICAL PROPERTIES OF REST-FRAME 250-μM-SELECTED GALAXIES

The best-fitting SEDs of the 34 SMGs are shown in Fig. B1. Evidence from X-ray studies suggest that many SMGs host an AGN (Alexander et al. 2005). Indeed some SMGs in our sample show excess emission in the rest-frame NIR, which may be due to dust heated to high temperatures by an obscured AGN (Hainline et al. 2011). The MAGPHYS SED models do not include a prescription for AGN emission and so we must assess the impact that AGN emission may have on the parameters. The details of this process and the results are discussed in Appendix C but in brief, we select galaxies at $z > 1$ with power-law emission in the NIR from the $S_{24}/S_{8.0}-S_{8.0}/S_{4.5}$ diagram from Ivison et al. (2004), with $S_{8.0}/S_{4.5} > 1.65$ (Coppin et al. 2010). We find 6/34 galaxies are classed as AGN in this way (AzLOCK.01, AzLOCK.10, AzTECJ100019+023206, LOCK850.04, LOCK850.15 and GN20[8]). Following the method of Hainline et al. (2011), we subtract a power law with $f_\lambda \propto \lambda^\alpha$, where $\alpha = 2$ or 3, from all photometry shortwards of 8 μm (observed), incrementally adjusting the power-law contribution at 8 μm to achieve the best fit.

In the following results, we use the best-fitting power-law subtracted values for the four AGN with weak power-law components (AzLOCK.1, AzLOCK.10, LOCK850.15 and GN20). We use the results derived using a power-law slope of $\alpha = 3$ as this provides the best fit to the data, except for the case of GN20 where the data are best fitted by a power-law slope of $\alpha = 2$. We exclude AzTECJ100019+023206 as the lack of reliable photometry makes the AGN power-law fraction difficult to constrain, and LOCK850.04 is excluded as the uncertainties on the parameters due to subtraction of the dominant power law are too large to make this galaxy a useful member of the sample. The subtraction of a power law from the photometry of the AGN hosts in all cases results in a better SED fit indicated by a lower χ^2. The galaxies with power-law emission

[8] Although the observed $S_{8.0}/S_{4.5}$ colour traces the rest-frame 1.6 μm stellar bump at $z \sim 4$, we retain GN20 in our AGN sample as Riechers et al. (2013) found that GN20 has an obscured AGN from power-law emission in the rest-frame MIR spectrum.

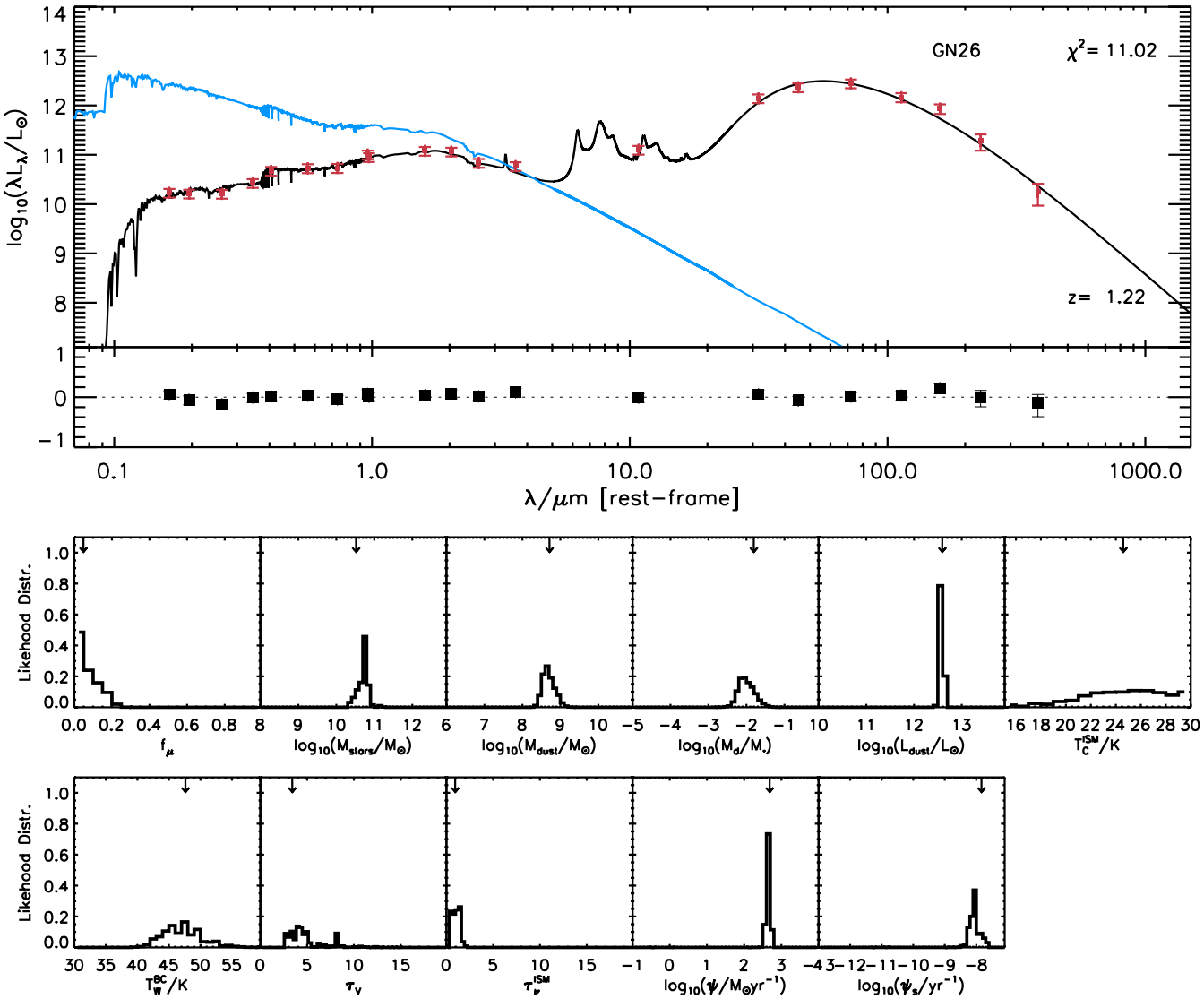

Figure 1. Top: example best-fitting rest-frame SED of a high-redshift submillimetre galaxy, with observed photometry (red points) from the rest-frame UV to the submillimetre. Errors on the photometry are described in Section 2.2. The black line is the best-fitting model SED and the blue line is the unattenuated optical model. Bottom: PDFs for each physical parameter are shown for this submillimetre galaxy, with the best-fitting model values shown as arrows above each parameter PDF. The parameters are (from left to right): f_μ, the fraction of total dust luminosity contributed by the diffuse ISM; $M_*/\mathrm{M}_\odot$, stellar mass; $M_\mathrm{d}/\mathrm{M}_\odot$, dust mass; M_d/M_* , dust-to-stellar mass ratio; $L_\mathrm{d}/\mathrm{L}_\odot$, dust luminosity; $T_\mathrm{C}^\mathrm{ISM}$/K, temperature of the cold diffuse ISM dust component; T_W^BC/K, temperature of the warm dust component in birth clouds; $\hat{\tau}_V$, total effective V-band optical depth seen by stars in birth clouds; $\hat{\tau}_V^\mathrm{ISM}$, effective V-band optical depth in the ambient ISM; $\psi/\mathrm{M}_\odot$ yr^{-1}, the SFR; and $\psi_\mathrm{S}/\mathrm{yr}^{-1}$, the SSFR. The SSFR and SFR are averaged over the last 10^7 yr, although in this example the result is insensitive to changes in the time-scale over which the SFR is averaged.

comprise a small minority of the SMG sample, and the choice of whether to subtract the power law or not, or exclude them from the sample, does not change our conclusions.

After subtracting the best-fitting power-law slope from the optical–MIR photometry, as expected we typically see a decrease in the stellar mass of the AGN-dominated SMGs. However, an increase in the stellar mass occurs in some cases because the optical depth increases (albeit with rather large uncertainty). The stellar mass changes by slightly more than the error represented by the 84th–16th percentile range on each individual galaxy PDF (on average ±0.11 dex). We find that the median-likelihood f_μ, SFR, SSFR and $\hat{\tau}_V$ move slightly but are typically within the error represented by the 84th–16th percentile range on each individual galaxy PDF.

We exclude LOCK850.17 and LESS17 from our final sample because there is a large discrepancy between the photometric and spectroscopic redshift. This was also noted for LOCK850.17 in Dye et al. (2008), who propose that the spectroscopic redshift is from a background source blended with a foreground galaxy which dominates the flux measurements. Furthermore, Simpson et al. (2014) found that LESS17 has a photometric redshift of $1.51^{+0.10}_{-0.07}$. We exclude GN20.2 as the low signal-to-noise optical–NIR photometry does not allow us to obtain reliable constraints on the physical parameters for this source. The final sample comprises 29 SMGs with $0.48 < z < 5.31$.

To create a low-redshift comparison sample, we fit the UV–millimetre SEDs of 18 869 low-redshift ($0.005 < z < 0.5$) H-ATLAS galaxies using a similar method to Smith et al. (2012b).

These sources are selected to have a reliability >0.8 of being associated with an optical counterpart in the SDSS *r*-band catalogue and have multiwavelength photometry from the GAMA survey (see Smith et al. 2012b). Updated PACS and SPIRE fluxes in all bands are utilized even if they are low signal-to-noise, as this provides more constraint on the SED than setting undetected fluxes to upper limits (Smith et al. 2013). To ensure that we only include galaxies which have good photometry, we reject 3856 galaxies which have a less than 1 per cent chance that their photometry is well described by the best-fitting model SED, see Smith et al. 2012b for details. Galaxies which are excluded from the sample have problems with AGN contamination or issues with photometry. This can happen where the optical photometry is not equivalent to 'total light' if the SEXTRACTOR source detection used by GAMA (Hill et al. 2011) deblended single objects, or had stellar contamination, for example. Given the wide parameter space of the MAGPHYS libraries, galaxies with physically plausible SEDs should be well fitted by our models.

In this study, we use the 15 013 galaxies at $0.005 < z < 0.5$ whose photometry is well described by the best-fitting model SED. We make two comparisons: one between all the low-redshift H-ATLAS galaxies and the SMGs in order to study the diversity of galaxies which are selected at approximately rest-frame ∼250 μm and secondly between a stellar mass-matched sample at high and low redshift in order to determine how the properties of massive SMGs differ over cosmic time.

To construct the stellar mass-matched sample, we split the SMG sample into median-likelihood stellar mass bins of 0.2 dex width and randomly picked galaxies in the same stellar mass bin from the H-ATLAS sample, such that both distributions matched. We pick the maximum number of H-ATLAS galaxies such that we can still approximately match the SMG stellar mass distribution (30 times the number of SMGs). Even so, there is a lack of H-ATLAS galaxies with the very highest stellar masses with 23/30 (77 per cent) of galaxies missing from the highest stellar mass bin centred on $10^{11.7}$ $M_{\odot}$. Of the total low-redshift stellar mass-matched sample (843 galaxies), only 3 per cent of galaxies are missing from the mass-matched sample. The final ∼ 250 μm rest-frame-selected sample comprises 29 SMGs ($\bar{z} = 2.13$) and 843 low-redshift galaxies from H-ATLAS ($\bar{z} = 0.26$) of a similar stellar mass to the high-redshift sample. The redshift distributions of the samples are shown in Fig. 2.

The samples investigated in this paper are not typical of the general galaxy population, but represent the most infrared-luminous galaxies at their respective redshifts. We note that the high-redshift SMG sample is not intended to be evolutionarily linked to the low-redshift H-ATLAS galaxies. SMGs are likely to rapidly exhaust their gas supply within a few hundred Myr, and are unlikely to be dusty enough to be detected in the H-ATLAS sample at low redshift. The low-redshift descendents of the SMGs are thought to be massive ellipticals (e.g. Eales et al. 1999; Simpson et al. 2014). We may glimpse a transitional period where once high-redshift dusty starbursts are transitioning on to the red sequence and yet still retain some ISM. Such dusty early-type galaxies have been observed in the H-ATLAS sample by Rowlands et al. (2012) and have comparable stellar masses to the SMG sample.

The selection effects in the high-redshift sample (e.g. the need for radio counterparts, requirement of spectroscopic redshifts and panchromatic SED coverage) are rather complex, which can result in a biased sample of SMGs. M12 have examined the selection effects in detail and conclude that high infrared luminosity ($L_{\rm IR} \geq 10^{12.5}$ $L_{\odot}$) SMGs with spectroscopic redshifts are representative of the parent SMG population, and the high-luminosity star-forming galaxy population in general. In Section 4.1, we therefore concentrate our analysis on these FIR-luminous SMGs, which are typically at $z > 1$. At lower FIR luminosities, the SMG sample shifts to lower redshift galaxies with cooler temperatures and less extreme properties, which produces some overlap between the SMG and low-redshift samples. Quantitative comparisons between the high- and low-redshift samples should therefore be interpreted within the selection functions of the samples.

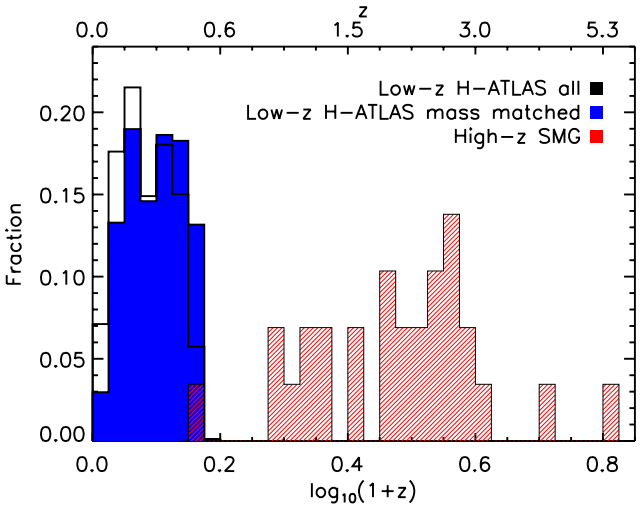

Figure 2. Redshift distribution of the entire low-redshift H-ATLAS sample (black open histogram), low-redshift mass-matched sample (blue solid histogram) and the SMGs (red hatched histogram). The redshift distribution of the 29 SMGs has a mean of $\bar{z} = 2.13$, the mean redshift of the 843 low-redshift galaxies with a similar stellar mass to the high-redshift sample is $\bar{z} = 0.26$, which is similar to that of the entire $z < 0.5$ H-ATLAS sample ($\bar{z} = 0.22$).

We show the median-likelihood physical parameters for each individual SMG with a good SED fit in Table D1. To compare the physical parameters of the high- and low-redshift dusty populations, we compute the stacked PDF of parameters derived from the SED fitting, which are shown in Fig. 3. For each parameter, we use the first moment of the stacked PDF to estimate the mean of the population, with the variance on the population taken from the second moment of the average PDF minus the mean squared. The error on the mean is simply the square root of the population variance, normalized by the square root of the number of galaxies in the sample. The mean values and errors on each PDF for the high- and low-redshift samples are summarized in Table 1, including parameters for the SMGs derived using both set of priors. We show the mean PDF for the high-redshift SMG sample using the standard priors, to reassure the reader that the trends observed between the low- and high-redshift samples are not driven by the use of different priors.

4.1 Comparison of parameters for high- and low-redshift populations

In this section, we compare the mean physical parameters for the high-redshift ($z > 1$) SMGs and the low-redshift mass-matched sample drawn from H-ATLAS. We note that using the whole low-redshift H-ATLAS sample in place of the mass-matched sample produces a negligible difference in our results.

Fraction of total dust luminosity contributed by the diffuse ISM: f_{μ}. The dust luminosity in most SMGs is dominated by the birth cloud component, whilst the dust luminosity in low-redshift galaxies is

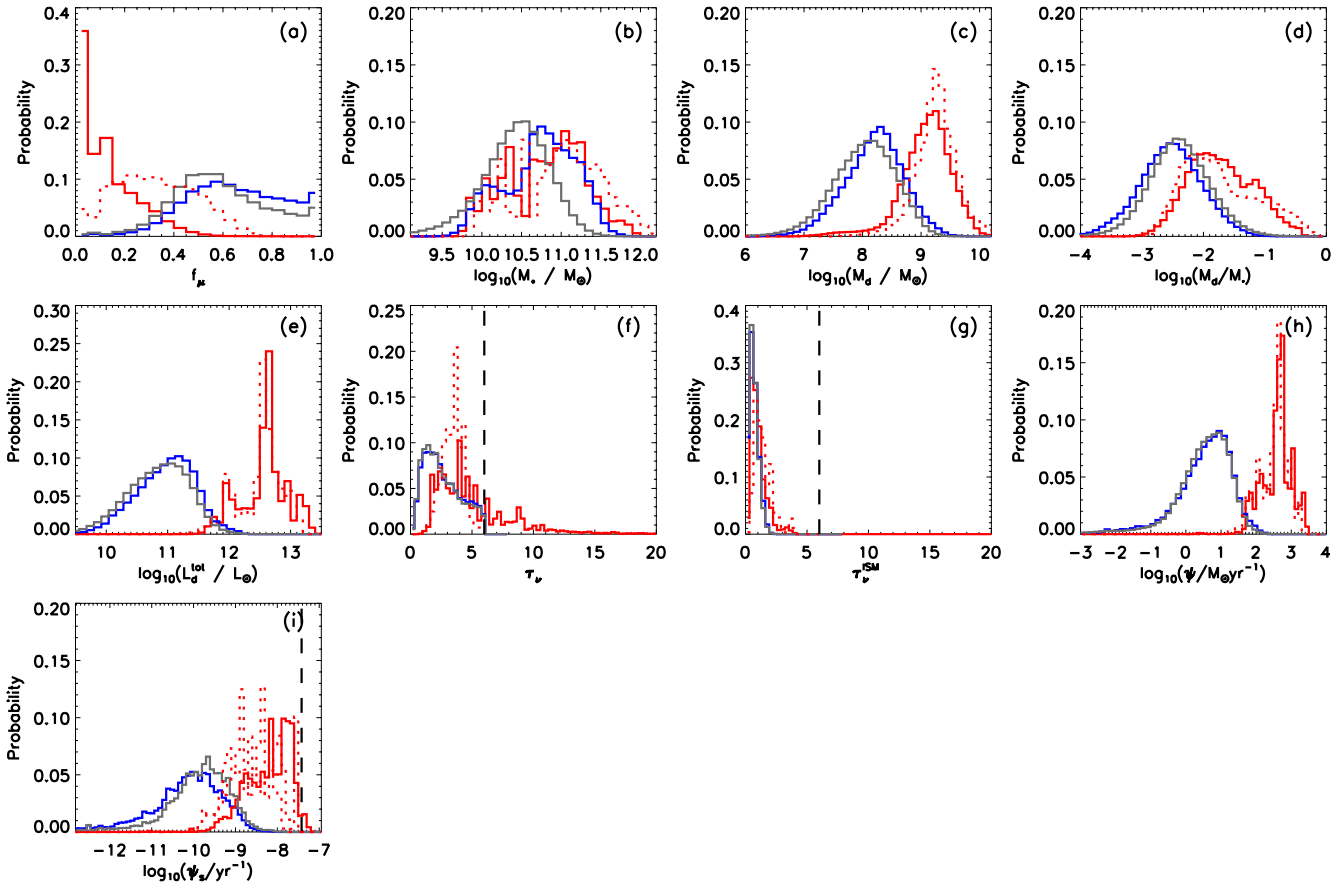

Figure 3. Mean PDFs of the entire $z < 0.5$ H-ATLAS sample (grey solid line), the low-redshift mass-matched sample (blue solid line) and high-redshift $z > 1$ SMGs (red solid line). We also show the mean PDF for the high-redshift SMG sample using the standard priors (red dotted line). The parameters are (from left to right): f_μ, the fraction of total dust luminosity contributed by the diffuse ISM; $M_*/\mathrm{M}_\odot$, stellar mass; $M_\mathrm{d}/\mathrm{M}_\odot$, dust mass; M_d/M_* , dust to stellar mass ratio; $L_\mathrm{d}/\mathrm{L}_\odot$, dust luminosity; $\hat{\tau}_V$, total effective V-band optical depth seen by stars in birth clouds; $\hat{\tau}_V^{\mathrm{ISM}}$, the total effective V-band optical depth in the ambient ISM $\psi/\mathrm{M}_\odot\ \mathrm{yr}^{-1}$, the SFR averaged over the last 10^7 yr; and $\psi_\mathrm{S}/\mathrm{yr}^{-1}$, the SSFR averaged over the last 10^7 yr. The ranges of each panel reflect the width of the priors for the SMG libraries. Where the prior range is different for the standard libraries, the edge of the prior space is marked with a black dashed line.

Table 1. Summary of mean physical properties of the samples examined in this paper derived from stacking PDFs for the different galaxy populations studied in this paper. The parameters are: f_μ, the fraction of total dust luminosity contributed by the diffuse ISM; $M_*/\mathrm{M}_\odot$, stellar mass; $M_\mathrm{d}/\mathrm{M}_\odot$, dust mass; M_d/M_* , dust to stellar mass ratio; $L_\mathrm{d}/\mathrm{L}_\odot$, dust luminosity; $\hat{\tau}_V$, total effective V-band optical depth seen by stars in birth clouds; $\hat{\tau}_V^{\mathrm{ISM}}$, effective V-band optical depth in the ambient ISM; $\psi^7/\mathrm{M}_\odot\ \mathrm{yr}^{-1}$, the SFR averaged over the last 10^7 yr; $\psi_\mathrm{S}{}^7/\mathrm{yr}^{-1}$, SSFR averaged over the last 10^7 yr; $\psi^8/\mathrm{M}_\odot\ \mathrm{yr}^{-1}$, the SFR averaged over the last 10^8 yr ; and $\psi_\mathrm{S}{}^8/\mathrm{yr}^{-1}$, the SSFR averaged over the last 10^8 yr.

Parameter	Low-redshift mass-matched sample (Standard prior)	$z > 1$ SMG sample (SMG prior)	$z > 1$ SMG sample (Standard prior)
f_μ	0.65 ± 0.01	0.13 ± 0.02	0.32 ± 0.02
$\log_{10}(M_*)$	10.73 ± 0.02	10.80 ± 0.10	10.97 ± 0.10
$\log_{10}(M_\mathrm{d})$	8.19 ± 0.02	9.09 ± 0.09	9.27 ± 0.07
$\log_{10}(M_\mathrm{d}/M_*)$	− 2.54 ± 0.02	− 1.71 ± 0.10	− 1.70 ± 0.12
$\log_{10}(L_\mathrm{d})$	10.96 ± 0.02	12.57 ± 0.07	12.50 ± 0.07
$\hat{\tau}_V$	2.7 ± 0.1	5.1 ± 0.6	3.4 ± 0.2
$\hat{\tau}_V^{\mathrm{ISM}}$	0.7 ± 0.1	1.0 ± 0.1	1.4 ± 0.1
$\log_{10}(\psi^7)$	0.51 ± 0.03	2.59 ± 0.08	2.50 ± 0.08
$\log_{10}(\psi_\mathrm{S}{}^7)$	− 10.22 ± 0.03	− 8.21 ± 0.11	− 8.47 ± 0.12
$\log_{10}(\psi^8)$	0.56 ± 0.03	2.53 ± 0.08	2.23 ± 0.07
$\log_{10}(\psi_\mathrm{S}{}^8)$	− 10.17 ± 0.03	− 8.27 ± 0.10	− 8.75 ± 0.09

dominated by the diffuse ISM (Fig. 3a). If the standard priors are used, the values of f_μ tend to be higher but we still find that the majority of the SMGs have f_μ<0.5.

Stellar mass: M_*. In Fig. 3(b), we find a mean stellar mass of $6.3^{+1.6}_{-1.3} \times 10^{10}$ $M_\odot$ for the $z > 1$ SMGs, in agreement with Hainline et al. (2011) and M12. Using Bruzual & Charlot (2003) models Michałowski et al. (2012b) found stellar masses for SMGs which were higher by a factor of 2−4 compared to those in this study. This difference in stellar mass is due to the use of different SFHs, stellar population models and the strength of the TP-AGB stars in the stellar population models. By design, the stellar mass of the low-redshift mass-matched sample ($5.5 \pm 0.2 \times 10^{10}$ $M_\odot$) is similar to that of the SMGs.

Dust mass: M_d. The $z > 1$ SMG sample has a mean dust mass of $1.2^{+0.3}_{-0.2} \times 10^9$ $M_\odot$ (Fig. 3c), similar to other studies of SMGs (Santini et al. 2010; Magdis et al. 2012; Simpson et al. 2014). The dust masses of the SMGs are around an order of magnitude higher than the low-redshift H-ATLAS galaxies, which have a mean dust mass of $(1.6 \pm 0.1) \times 10^8$ $M_\odot$. Furthermore, there is a dearth of galaxies in the low-redshift sample with dust masses as large as the dustiest SMGs ($M_d > 2.5 \times 10^9$ $M_\odot$). It is not surprising that a high-redshift submillimetre sample has a higher average dust mass, since moderate dust masses are not detectable at high redshifts with *Herschel*. However, this selection effect does not account for the much larger space density of the dustiest galaxies at high redshift, since these would have been detected in H-ATLAS should they exist at lower redshift. This is consistent with the observed strong evolution in the dust content of massive, dusty galaxies with redshift, in agreement with Dunne & Eales (2001), Dunne et al. (2003), Eales et al. (2010b), Dunne et al. (2011), Bourne et al. (2012) and Symeonidis et al. (2013).

Dust-to-stellar mass: M_d/M_*. The M_d/M_* values of $z > 1$ SMGs in Fig. 3(d) typically range from 0.01 to 0.05, with a mean of $0.019^{+0.005}_{-0.004}$, similar to that found by Santini et al. (2010). While Santini et al. (2010) found that SMGs have a factor of 30 higher M_d/M_* compared to a sample of normal spirals from SINGS, we find our SMGs to be only a factor of 7 more dusty relative to their stellar mass compared to low-redshift H-ATLAS galaxies. This disparity may be because Santini et al. (2010) compare to a sample of very local galaxies, whereas the H-ATLAS sample is selected at 250 μm and covers a greater range in redshift, in which evolution in dust mass has already occurred (Dunne et al. 2011; Bourne et al. 2012).

Dust luminosity: L_d. The dust luminosities of the low- and high-redshift samples are significantly different (Fig. 3e). The mean of the low-redshift sample is $9.2^{+0.4}_{-0.3} \times 10^{10}$ $L_\odot$, whereas the SMGs have an average dust luminosity a factor of 40 higher. The mean total dust luminosity of the high-redshift SMGs ($3.7^{+0.7}_{-0.6} \times 10^{12}$ $L_\odot$) is in good agreement with M12.

Optical depth: $\hat{\tau}_V$, $\hat{\tau}_V^{\rm ISM}$. As shown in Fig. 3(f) and (g), the total effective *V*-band optical depth seen by stars in birth clouds ($\hat{\tau}_V$) is around a factor of 2 higher for the SMG sample compared to low-redshift H-ATLAS galaxies, although the optical depth in the diffuse ISM ($\hat{\tau}_V^{\rm ISM}$) is similar for the two samples. These results are consistent with other studies which found that SMGs are very obscured compared to local galaxies, but are not as obscured as local ULIRGs (Menéndez-Delmestre et al. 2009). This is the likely reason behind the higher f_μ values observed in SMGs.

Star formation rate: SFR. The SFR of the SMGs (averaged over the last 10^7 yr) ranges from 62 to 2200 $M_\odot$ yr^{-1}, but there is a strong trend of SFR with redshift. For SMGs at $z > 1$, the mean is 390^{+80}_{-70} (Fig. 3h), in agreement with other recent studies of similar samples (Banerji et al. 2011; Lo Faro et al. 2013; Simpson et al. 2014). We note that because we exclude six SMGs where the submillimetre emission may originate from multiple sources at the same redshift, the sample may be biased against systems undergoing major mergers, which tend to have the highest SFRs. The average SFR of the SMGs is around 120 times that of the low-redshift sample (SFR = 3.3 ± 0.2 $M_\odot$ yr^{-1}). The lack of highly star-forming galaxies in the low-redshift sample is not a volume effect, as the comoving volume probed by the H-ATLAS Phase 1 data is 1.1×10^8 Mpc^3, which is comparable to the comoving volume of the SMG sample from the combined SPIRE survey areas of GOODS-N, ECDFS, COSMOS and Lockman Hole (1.3×10^8 Mpc^3 for $1.0 < z < 5.31$). SMGs at fixed stellar mass have higher SFRs at higher redshift, which reflects the strong evolution in characteristic SFR in galaxies out to $z \sim 2$ (Sobral et al. 2013).

Specific star formation rate: SSFR. The mean SSFR of the $z > 1$ SMG sample in Fig. 3(i) is $6.1^{+1.7}_{-1.3} \times 10^{-9}$ yr^{-1}, which implies a doubling time of 160 Myr. The SSFR values derived from our SED fitting are in broad agreement with those from M12 derived from the FIR luminosity, albeit with large scatter. The average SSFR of the SMGs from the MAGPHYS SED fitting is 100 times greater than the mean SSFR of the low-redshift sample, which has an average SSFR of $6.1^{+0.5}_{-0.4} \times 10^{-11}$ yr^{-1}. The difference in the mean PDFs when using the SMG and standard priors for the SFR and SSFR averaged over the last 10^7 yr are 0.09 and 0.26 dex, respectively. When using the SMG priors, these results are not sensitive to the time-scale over which the (S)SFR is averaged, although with the standard priors the mean SMG (S)SFR is lower when averaging over a longer time-scale of 10^8 yr. This is due to the birth cloud time-scale being fixed at 10^7 yr in the standard model, which is unable to generate the high optical depths (and hence obscured SFRs) required to fit all of the SMG SEDs. However, the choice of prior or time-scale over which to average SFR does not change the conclusion that dusty galaxies at high redshift are forming more stars than dusty galaxies of a similar stellar mass at low redshift.

4.2 SEDs of dusty galaxies at low and high redshift

We now investigate the shapes of the SEDs of the galaxies in our sample. In Fig. 4, we show the median SEDs of all H-ATLAS galaxies, mass-matched H-ATLAS galaxies and $z > 1$ SMGs. The median SEDs are derived using a similar method to that presented Smith et al. (2012b), but with ∼10 times as many sources. Since we are comparing stacked SEDs of a similar stellar mass, the SEDs are normalized at 2.2 μm. In Fig. 4, the median SED of the stellar mass-matched sample is broadly consistent with the stack of the full H-ATLAS sample at wavelengths >4000 Å. At shorter wavelengths, the mass-matched sample is redder which is most likely due to it sampling the highest mass end of the H-ATLAS distribution which has a greater contribution from lower SSFR objects (see Fig 3). The MIR region in the H-ATLAS-stacked SED shows the largest variation, as each best-fitting SED is only weakly constrained by the model priors; however, Smith et al. (2012b) showed that a lack of MIR data does not affect the results derived from the SED fitting. The stacked SMG SED is much more obscured, hot and luminous compared to the low-redshift H-ATLAS SED. Whilst we note that we could be biased towards warmer SMGs in our sample due to the need for at least one PACS/SPIRE detection, M12 have shown

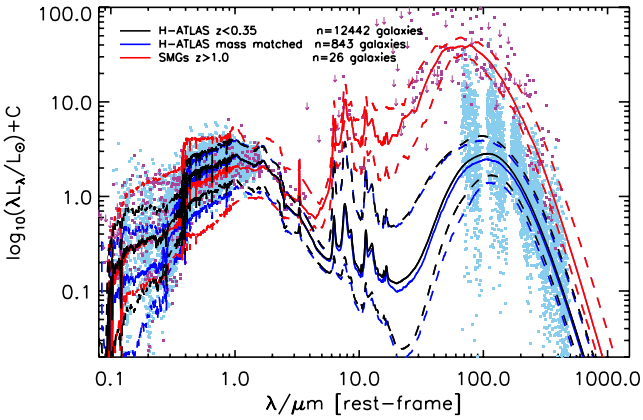

Figure 4. Median-stacked SEDs of the entire H-ATLAS sample with $z < 0.35$ based on the updated Smith et al. (2012b) H-ATLAS SED fits (black), the low-redshift mass-matched sample (blue) and the $z > 1$ SMGs (red). The thick lines show the median of the best-fitting MAGPHYS SEDs and the dotted lines show the 1σ spread around the median SED. The red and blue points show the deredshifted and normalized observed photometry for the SMGs and the low-redshift mass-matched sample. The SEDs are normalized at rest-frame 2.2 μm. The stellar mass-matched sample is broadly consistent with the stack of the full H-ATLAS sample at wavelengths >4000 Å. The stacked SMG SED is much more obscured, hot and luminous compared to the low-redshift H-ATLAS SED.

that the dominant selection bias in the SMG sample is due to the need for (sub)mm and radio detections. This striking visual confirmation of the shift in SED shape was implied by Lapi et al. (2011) to occur in the submillimetre-selected population in the interval $0.5 < z < 1.5$.

In Fig. 5, we show the median SEDs of the $z > 1$ SMGs and the updated H-ATLAS empirical SED templates from Smith et al. (2012b), binned by best-fitting SSFR and dust luminosity. In Fig. 5(a), there is a strong trend for the SEDs of $z < 0.35$ H-ATLAS galaxies to become bluer in the optical with increasing SSFR and hotter in the dust continuum (see also Smith et al. 2012b). However, the SMG bin (which has minimal overlap in SSFR with the low-redshift H-ATLAS galaxies) shows quite a break in the optical–UV trend, with the SMG SED being much redder and more obscured. The trend for warmer dust continuum continues, together with a marked increase in the ratio of IR to optical–UV continuum. Thus, for a modest increase in SSFR, the stacked SMG SED looks very different to the most actively star-forming galaxies at $z < 0.35$ in H-ATLAS. Most H-ATLAS galaxies have f_μ values which indicate that around half of their L_d is contributed by birth clouds, while SMGs have much lower values of f_μ suggesting that ≥80 per cent of their L_d is produced in obscured star-forming regions. The change in SED shape could be due to SMGs having more birth cloud relative to diffuse ISM luminosity. In Fig. 6(a), we see a steady decrease in the value of f_μ as SSFR increases, such that the highest SSFR bin for $z < 0.35$ H-ATLAS sources has a similar f_μ to the SMGs. The sudden change in the optical–UV SED between the highest SSFR H-ATLAS galaxies and the SMGs cannot be due to a sharp change in f_μ; rather it must be due to a physical difference in the structure of birth clouds in SMGs. Our SED fitting prefers that the birth clouds in SMGs have a higher optical depth on average (see Fig. 6b), and the stars are also able to spend longer in them (suggesting they last longer before disruption). We return to this subject in Section 4.4.

For SEDs binned by dust luminosity in Fig. 5(b), the SEDs show a more steady trend of becoming redder in the optical with increasing dust luminosity and also warmer in the infrared above a dust luminosity of $\sim 10^{11}$ L$_\odot$ (consistent with Smith et al. 2012b). There is no marked difference in the trend once the SMG bin is reached, as is apparent for the SSFR binning.

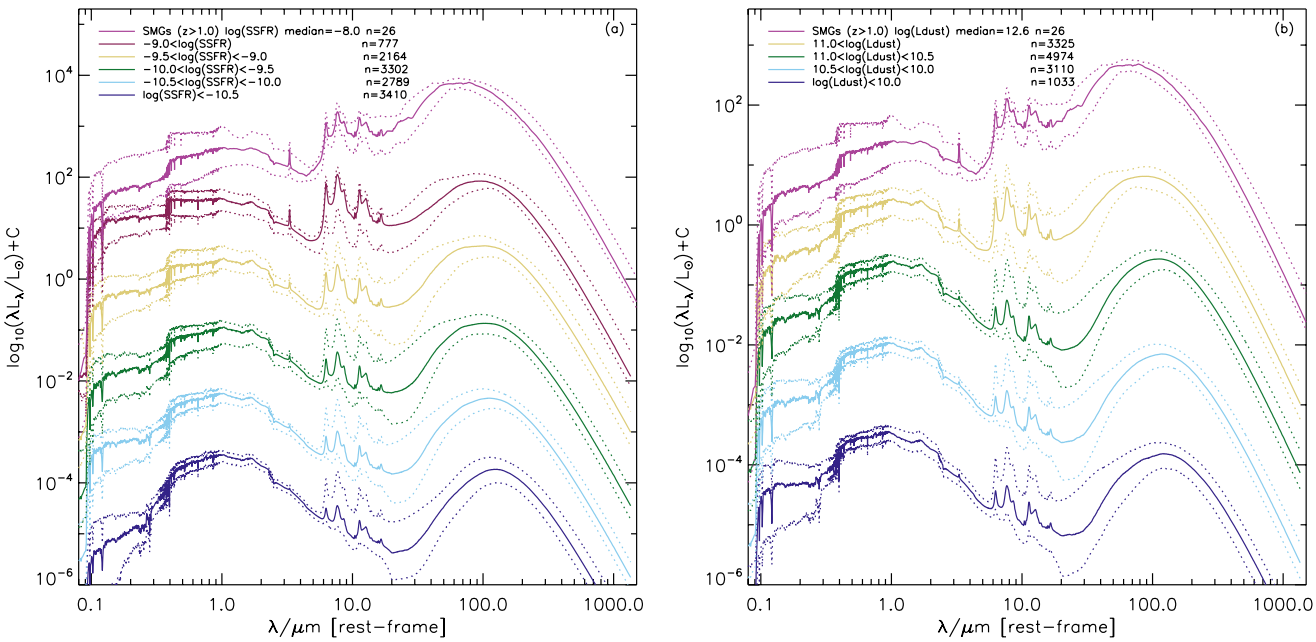

Figure 5. (a) Median-stacked SEDs in bins of best-fitting SSFR for the $z > 1$ SMGs (upper red SED) and the entire $z < 0.35$ H-ATLAS sample, based on the updated Smith et al. (2012b) H-ATLAS SED fits. The SEDs become bluer in the optical and have a hotter dust continuum with increasing SSFR. The stacked SMG SED shows a redder optical continuum due to increased obscuration compared to the H-ATLAS galaxies. (b) Stacked SEDs in bins of best-fitting dust luminosity. The SEDs have a redder optical continuum with increasing L_d and increase in dust temperature for L > 10^{11}L$_\odot$. The dotted lines show the 1σ spread around the median SED.

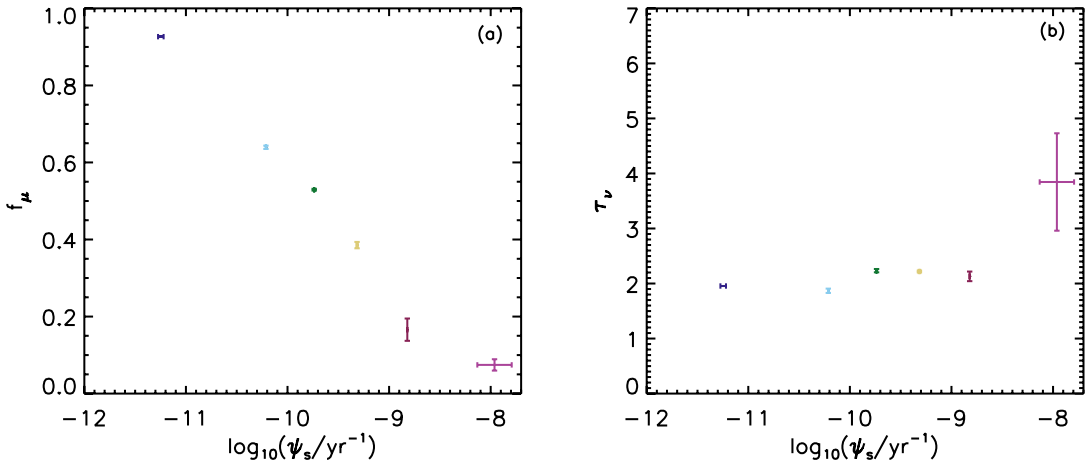

Figure 6. The relationship between the median values of the best-fitting f_μ and SSFR (a) and $\hat{\tau}_V$ and SSFR (b) in each SSFR bin in Fig. 5. Error bars indicate the standard error on the median for each bin using the method in Gott et al. (2001). The average f_μ for the SMGs (red point) does not show a sharp change compared to the f_μ values of the low-redshift sample in bins of SSFR. The values of $\hat{\tau}_V$ are relatively constant with increasing SSFR for the low-redshift H-ATLAS galaxies, but there is a sharp increase in $\hat{\tau}_V$ for the SMGs.

4.3 Infrared luminosity as a star formation tracer in SMGs

Studies of infrared- and SMGs have traditionally relied on using the re-radiated energy from dust at 8-1000 μm as a proxy for SFR. The seminal work by Kennicutt (1998, hereafter K98) explains in detail the basis of this relationship and provides a calibration (see also Kennicutt et al. 2009). The main requirement for dust luminosity to be a good tracer of SFR is that the bulk of the star formation is obscured and the dust emission is produced from absorption of photons produced by massive stars.[9] Since MAGPHYS aims to account for both obscured (radiated in the FIR) and unobscured (radiated in the UV) star formation, *and* also accounts for that fraction of L_d which is heated by older stellar populations, it is instructive to look at the correlation of the MAGPHYS SFR with L_d (Fig. 7). Galaxies with low f_μ lie on the K98 relation, which means that for SMGs, this relation is a reliable way of predicting the SFR from the total infrared luminosity – as expected given their high obscuration. Galaxies with a significant contribution to the infrared luminosity from the diffuse ISM (mostly powered by stars older than 10 Myr) lie further from the K98 relation, and are mostly low-redshift H-ATLAS galaxies. Using L_d and the K98 relation will therefore overestimate the SFR in galaxies where the dust luminosity is produced mainly in the diffuse ISM component (i.e. high f_μ). The robustness of MAGPHYS SFR relative to a number of well-used SFR tracers is investigated further in a study by Smith et al. (in preparation).

4.4 Understanding the ISM in SMGs and low-redshift galaxies

The mass of dust and SFR are correlated in galaxies (da Cunha et al. 2010a); such a relationship might be expected if dust is a tracer of the gas content in galaxies (Eales et al. 2012; Scoville 2013), as gas mass and SFR are linked by the Kennicutt–Schmidt relation (K98). To investigate this idea, we show in Fig. 8(a) the SFR from MAGPHYS versus the dust mass. In these plots, we also include local ULIRGS fitted using MAGPHYS in the study by da Cunha et al. (2010b). The $z > 1$ SMGs and local ULIRGs follow a parallel but offset relationship

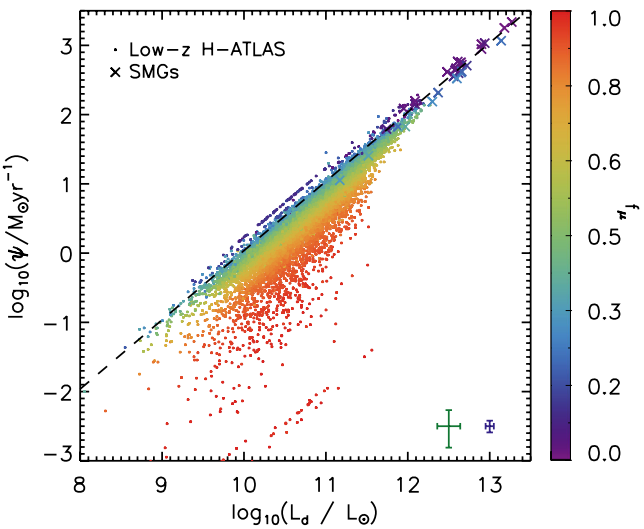

Figure 7. The relation between median-likelihood dust luminosity and SFR for the low-redshift H-ATLAS galaxies (dots) and SMGs (crossed). Points are coloured by the value of f_μ. The dashed line shows the relation between SFR and total infrared luminosity (integrated from 8−1000 μm) from K98. The error bars indicate the median 84th–16th percentile range from each individual parameter PDF; the green and blue error bars correspond to the low-redshift H-ATLAS and SMG samples, respectively. Galaxies with low f_μ lie on the K98 relation, which means that for SMGs, this relation is a reliable way of predicting the SFR from the total infrared luminosity. For galaxies with a significant contribution to the infrared luminosity from the diffuse ISM, the K98 relation will produce an overestimate of the SFR from L_d.

from the H-ATLAS $z < 0.5$ sources. Interestingly, the $z < 1$ SMGs lie closer to the H-ATLAS sources than to the other SMGs. If dust is a good tracer of gas, this implies that high-redshift SMGs and local ULIRGS have more SFR per unit gas mass than the $z < 0.5$ H-ATLAS galaxies. The quantity $\mathrm{SFR}/M_\mathrm{d}$ is therefore inversely proportional to a gas-depletion time-scale, τ_g, (or proportional to a star formation efficiency) under the assumption of a roughly uniform gas-to-dust ratio for galaxies in this sample. Fig. 8(a) implies shorter gas-depletion time-scales for high-redshift SMGs and ULIRGs than

[9] There is a slightly different calibration (Hao et al. 2011) if UV emission is being added to the infrared luminosity in order to capture both the obscured and unobscured component.

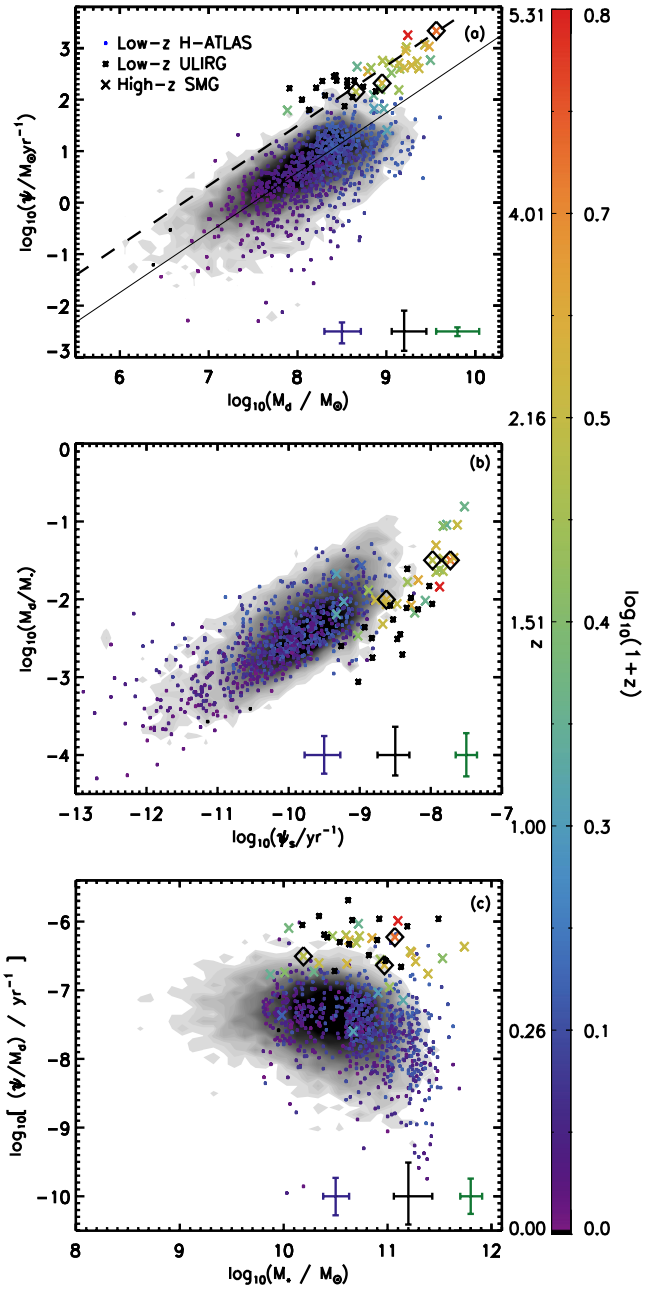

Figure 8. (a) The relation between median-likelihood SFR and dust mass, (b) dust-to-stellar mass ratio and SSFR, and (c) SFR/$M_{\rm d}$ and stellar mass for SMGs, the mass-matched low-redshift sample and low-redshift ULIRGs (crosses, dots and black stars, respectively). The shaded contours show the locus of the main H-ATLAS sample. The SFR and SSFR are averaged over the last 10^7 yr. Points are coloured by redshift. Open black diamonds indicate the three SMGs in our sample whose FIR photometry may be confused. The error bars indicate the median 84th–16th percentile range from each individual parameter PDF; the blue, black and green error bars correspond to the low-redshift H-ATLAS, ULIRG and SMG samples, respectively. In panel (a), the solid line is the fit to the H-ATLAS sample and the dashed line is the fit to the $z > 1$ SMGs and low-redshift ULIRGs, keeping the slope fixed to that of the H-ATLAS sample.

for more 'normal' galaxies at $z < 0.5$ (Tacconi et al. 2008; Genzel et al. 2010).

Such differences between SMGs and 'normal' star-forming galaxies have been found in previous studies of gas and SFR which use CO to trace the molecular gas (Tacconi et al. 2008; Dannerbauer et al. 2009; Daddi et al. 2010; Genzel et al. 2010), but see also Ivison et al. (2011). Fitting to the samples in Fig 8 (a) for the $z < 0.5$ H-ATLAS galaxies, and the $z > 1$ SMGs[10] and local ULIRGs gives

$$\log_{10}\ \mathrm{SFR} = 1.16\log_{10} M_{\rm d} - 7.81 \quad \text{for } z > 1 \text{ SMGs and low-}z \text{ ULIRGs,}$$
$$\log_{10}\ \mathrm{SFR} = 1.16\log_{10} M_{\rm d} - 8.72 \quad \text{for } z < 0.5\ \mathrm{H-ATLAS.} \qquad (1)$$

These have the same slope as that fitted to the $L_{\rm FIR}$[11] versus $L'_{\rm CO(1-0)}$ relationship of Genzel et al. (2010; hereafter G10). Since $L_{\rm FIR}$ should be proportional to SFR for the sources in G10 (see Section 4.3), we can infer that dust mass appears to trace molecular gas (for galaxies selected in the submillimetre) at least as well as $L'_{\rm CO(1-0)}$. To convert $L'_{\rm CO(1-0)}$ into a mass of molecular hydrogen, we must assume a conversion factor ($\alpha_{\rm CO}$), which depends on the dynamical state of the gas, and potentially also the metallicity (G10, Leroy et al. 2011; Narayanan et al. 2012; Sandstrom et al. 2013). Galaxies with strong nuclear starbursts, or which are mergers (e.g. local ULIRGs), are found to often have a lower $\alpha_{\rm CO}$ (Solomon et al. 1997; Downes & Solomon 1998; Yao et al. 2003) due to their gas being in a smoother, more diffuse state; no longer acting like an ensemble of virialized self-gravitating clouds.[12] Typically, authors have used the lower 'local ULIRG' value, $\alpha_{\rm CO} = 0.8\text{-}1.0\,\mathrm{M_\odot\,(K\,km\,s^{-1}\,pc^2)^{-1}}$ when studying high-redshift SMGs, under the assumption that their high infrared luminosities are also powered by compact starbursts, leading to similar conditions in the gas. While this appears to be appropriate in many cases (Tacconi et al. 2006, 2008; Magdis et al. 2011; Magnelli et al. 2012b), there are significant caveats about using it 'wholesale' for any SMG (Ivison et al. 2011; Papadopoulos et al. 2012; Bothwell et al. 2013). In particular, the latter authors warn that the mass of dense gas in these systems may be underestimated when using the standard ULIRG value for $\alpha_{\rm CO}$ and when only using lower excitation CO lines ($J < 3$).

In light of these outstanding issues, we will treat the conversion of CO luminosity to gas mass as an uncertain step and highlight any impacts of choosing a particular value of $\alpha_{\rm CO}$ on our conclusions. Using an $\alpha_{\rm CO} = 0.8\text{–}3.2\,\mathrm{M_\odot\,(K\,km\,s^{-1}\,pc^2)^{-1}}$ for SMGs/ULIRGS and normal star-forming galaxies, respectively, we can translate $L'_{\rm CO(1-0)}$ in the G10 relationship to $M_{\rm H_2}$, using $M_{\rm H_2} = 1.36\,\alpha_{\rm CO}\,L'_{\rm CO(1-0)}\ \mathrm{M_\odot}$(where the factor 1.36 accounts for the mass of helium). We translate the y-axis of the G10 relation using the K98 relationship: $L_{\rm IR} = 10^{10}$ SFR for a Chabrier IMF, and follow G10 in converting $L_{\rm FIR}$ to $L_{\rm IR}$[13] with a factor of 1.3. We can thus express the G10 relationships as

$$\log_{10}\ \mathrm{SFR} = 1.15\log_{10} M_{\rm H_2} - 9.30 \quad \text{for } z > 1 \text{ SMGs and low-}z \text{ ULIRGs,}$$
$$\log_{10}\ \mathrm{SFR} = 1.15\log_{10} M_{\rm H_2} - 10.60 \quad \text{for SFGs.} \qquad (2)$$

[10] Where we keep the slope fitted to the SMGs/ULIRG sample the same as the low-redshift sample.
[11] Integrated from 50−300 μm.
[12] An assumption which underlies the 'standard' conversion from $L'_{\rm CO(1-0)}$to $M_{\rm H_2}$.
[13] Integrated from 8-1000 μm.

We now have a relationship between SFR and dust mass in our samples and a relationship between SFR and molecular gas (as traced by CO) from G10 for comparable samples of SMGs/ULIRGs and normal star-forming galaxies. At a given gas-to-dust ($G_{\rm d}$) ratio, these two relationships (SFR versus $M_{\rm H_2}$ and SFR versus $M_{\rm d}$) will be equivalent. This happens at $G_{\rm d} = 30-150$ for SMGs (depending on the choice of $\alpha_{\rm CO}$) and $G_{\rm d} = 80$ for normal star-forming galaxies (the $z < 0.5$ H-ATLAS sample). These values are consistent with observations of high-redshift SMGs (Kovács et al. 2006; Swinbank et al. 2014) and star-forming galaxies in the local Universe (Seaquist et al. 2004; Draine et al. 2007; Leroy et al. 2011; Cortese et al. 2012; Sandstrom et al. 2013).

Not only does this comparison suggest that dust is as good a tracer of molecular gas as CO, but the consistency of the implied gas-to-dust ratios with observations of gas and dust in individual objects also suggests that the dust masses from MAGPHYS are reasonable and that evolution in $\kappa_{\rm d}$, the dust mass absorption coefficient, is not responsible for the shift in the SMGs relative to the H-ATLAS sources in Fig 8 (a). In fact, for a change in $\kappa_{\rm d}$ to explain this shift, the dust masses of the SMGs and ULIRGs would need to be higher by a factor 5 to bring them on to the same relation as the $z < 1$ galaxies. This would produce extremely high $M_{\rm d}/M_*$ values and very low inferred $G_{\rm d}$ from observations of CO, none of which are physically sensible given chemical and dust evolution modelling (Rowlands et al. 2014).

In Fig. 8(b), we plot $M_{\rm d}/M_*$ as a function of SSFR, which essentially normalizes the first plot by stellar mass so that we can compare the 'specific' quantities. The addition of SMGs allows us to extend the investigation of the $M_{\rm d}/M_*$ –SSFR relation to higher redshifts, beyond that studied in da Cunha et al. (2010a) and Smith et al. (2012b). Again using $M_{\rm d}$ as a proxy for gas mass, the y-axis ($M_{\rm d}/M_*$) is proportional to $f_{\rm g}/(1 - f_{\rm g})$, where $f_{\rm g}$ is the baryonic gas fraction ($f_{\rm g} = M_{\rm g}/[M_{\rm g} + M_*]$). Galaxies at the same horizontal position in this figure are thus equally 'gas rich'.[14] From Fig. 8(b), it is clear that SMGs are on average more 'gas rich' than the lower redshift H-ATLAS galaxies *and* the local ULIRGs (this agrees with detailed studies using CO; e.g. Tacconi et al. 2006; Geach et al. 2011; Bothwell et al. 2013). It is also apparent that the local ULIRGs have significant overlap in gas fraction with the H-ATLAS galaxies.

There is once again a significant offset in the locus of the $z > 1$ SMGs and local ULIRGs compared to the lower redshift H-ATLAS galaxies, such that at the same gas fraction, SMGs/ULIRGs have more star formation activity than 'normal' star-forming submillimetre-selected sources. This is an important point as it means that 'gas richness' alone cannot explain the offset between the samples in Fig. 8(a) – something else must happen in SMGs to push them into a more rapid and efficient conversion of their gas supply into stars. Recalling the change in optical SEDs between normal star-forming galaxies and SMGs from Section 4.2, it is likely that the physical changes in the ISM which lead to enhanced star formation efficiency are also the cause of the increased obscuration in the UV/optical. Observations of local ULIRGs have shown that high-density gas components ($N_{\rm H_2} > 10^5$ cm^{-3}) are dominant (Gao & Solomon 2004), and this is thought to be responsible for their high star formation efficiencies (Greve et al. 2009). At high redshift, galaxies are generally more gas rich (as we see from Fig 8b), and simulations of turbulent gas-rich discs have shown that they are dynamically unstable to fragmentation and collapse on a large scale (Elmegreen & Burkert 2010). This situation occurs on smaller scales in local ULIRGs, but which requires a major merger to initiate the instability in local galaxies (Barnes & Hernquist 1991, 1996; Mihos & Hernquist 1994, 1996).

The star-forming clumps in high-redshift SMGs are distributed over larger spatial scales (∼2 kpc) than those in local ULIRGs (50−200 pc), though the physical conditions inside them appear to be similar (Swinbank et al. 2011). The clumps appear in simulations and can last for $\sim 10^8$ yr, possibly due to the higher pressure in the ISM in SMGs/ULIRGs and high-redshift gas-rich systems (Genzel et al. 2008; Swinbank et al. 2011; Bournaud et al. 2014). Such large, dense and long-lived star-forming regions may be the reason for the high obscuration in these systems (recall that we needed to adjust the birth cloud time-scale parameter in MAGPHYS to achieve good fits). While mergers at high redshift will certainly produce the instability required to promote the collapse of the disc into large and dense clumps (Bournaud et al. 2011; Hayward et al. 2011), it is not clear that they are necessary in all cases.

Recalling that SFR/$M_{\rm d}$ is inversely proportional to a gas-depletion time-scale, Fig. 8(c) shows our proxy for $1/\tau_{\rm g}$ (or star formation efficiency) as a function of stellar mass. The star formation efficiency of SMGs and local ULIRGs show no trend with stellar mass, and have much shorter gas-depletion time-scales (higher star formation efficiencies) than the low-redshift sample at all stellar masses. Using the mean SFR and dust mass of SMGs from Section 4.1 and the $G_{\rm d}$ inferred from equating our relationships with those of G10, we estimate $\tau_{\rm g} \sim 90-460$ Myr for the $z > 1$ SMGs. The gas-depletion time-scales of the $z < 1$ SMGs are consistent with the low-redshift H-ATLAS galaxies, which have $\tau_{\rm g} \sim 4$ Gyr (using $G_{\rm d} = 80$ inferred from equations 1 and 2). The low-redshift H-ATLAS sample shows a slight trend, such that more massive galaxies have longer gas-depletion time-scales. Some of these low-efficiency galaxies are passive and not actively forming stars (Rowlands et al. 2012); however, removing all sources with SSFR $<10^{-11}$ yr^{-1} does not change the overall trend. The relation between star formation efficiency and stellar mass mirrors that seen between SSFR and stellar mass for the $z < 0.5$ galaxies.

To explain the offset between the SMGs and H-ATLAS galaxies as a result of metallicity differences (and therefore gas-to-dust ratio changes) would require evolution of the mass–metallicity relationship of the order of a dex or more from $z = 0.5$ to $z \sim 2-3$. This evolution in metallicity is not observed (Mannucci et al. 2010; Stott et al. 2013). Since similar offsets between star-forming galaxies and SMGs are found in studies which rely on CO as a gas mass tracer (Tacconi et al. 2006, 2008; Daddi et al. 2010; G10; Bothwell et al. 2013), we conclude that these differences between these galaxy populations are genuine.

4.5 The nature of star formation in SMGs

MAGPHYS also produces a best-fitting SFH for each galaxy, which is normalized to reproduce the best-fitting stellar mass from the SED fit. While these SFHs are not unique solutions (see Rowlands et al. 2014 for a discussion), it is still instructive to see which mode of star formation is fitted in these sources. Fig. E1 shows the SFHs of the SMG sample. Most of them could be described as 'bursts' of star formation, either because they have a short elevated SFR near the current age, or because their SFHs are so short and extreme that they can be considered a burst. The same conclusion was found by da Cunha et al. (2010b) in their study of local ULIRGs. Notably, the $z < 1$ SMGs are those with the least current star formation in the SMG sample and had their last burst some time ago, consistent

[14] Under the assumption that they have the same average gas-to-dust ratio.

with their similarity to the <0.5 H-ATLAS galaxies. As expected, SMGs are therefore likely to rapidly exhaust their gas supply within a few hundred Myr (Simpson et al. 2014, and references within).

5 CONCLUSIONS

We have presented the physical properties and SEDs of a rest-frame 250-μm-selected sample of massive, dusty galaxies, in the range $0 < z < 5.3$. The sample consists of a compilation of 29 high-redshift SMGs with photometry from M12 and 843 dusty galaxies at $z < 0.5$ from the *Herschel*-ATLAS, selected to have a similar stellar mass to the SMGs. Both samples have panchromatic photometry from the rest-frame UV to the submillimetre, which allowed us to fit SEDs to derive statistical constraints on galaxy physical parameters using an energy balance technique. We compared the physical properties of the high- and low-redshift samples and found significant differences in the SMG populations. Our main results are as follows.

(i) The sample of $z > 1$ SMGs have an average SFR of 390^{+80}_{-70} $M_\odot$ yr^{-1} which is around 120 times that of the low-redshift sample matched in stellar mass to the SMGs (SFR $=3.3 \pm 0.2$ $M_\odot$ yr^{-1}). This is consistent with the observed evolution in characteristic SFR of galaxies out to $z \sim 2$. The SMGs harbour an order of magnitude more dust ($1.2^{+0.3}_{-0.2} \times 10^9$ $M_\odot$), compared to $(1.6 \pm 0.1) \times 10^8$ $M_\odot$ for low-redshift dusty galaxies selected to have a similar stellar mass.

(ii) From the SED analysis, we find that a large fraction of the dust luminosity in SMGs originates from star-forming regions, whereas at lower redshifts, the dust luminosity is dominated by the diffuse ISM. This means that for SMGs the SFR can be reliably predicted from the K98 calibration between FIR luminosity and SFR. Where the dust luminosity is produced mainly by the diffuse ISM component, the K98 relation will overestimate the SFR, which is the case for the majority of low-redshift H-ATLAS galaxies.

(iii) The median SED of the SMGs is more luminous, has a higher effective temperature and is more obscured, with stars in birth clouds experiencing a factor of ∼2 more obscuration compared to the median low-redshift H-ATLAS SED. There is a sudden change in the optical–UV SED between the highest SSFR H-ATLAS galaxies and the SMGs, which cannot be due to a sharp change in the contribution to the total dust luminosity from birth clouds. Since the effective optical depth in SMGs is higher than in H-ATLAS galaxies, the change in SED shape may be due to a physical difference in the structure of birth clouds in SMGs.

(iv) We find that at the same dust mass the SMGs are offset by 0.9 dex towards a higher SFR compared to the low-redshift H-ATLAS galaxies. This is not only due to the higher gas fraction in SMGs but also because they are undergoing a more efficient mode of star formation. The offset cannot be explained by differences in the metallicities between the samples or variations in the dust emissivity.

(v) The offset in SFR and dust mass between the SMGs and low-redshift galaxies is similar to that found in CO studies. Due to the consistency between observations of gas and dust in individual SMGs and the gas-to-dust ratios implied by the ratio of FIR to CO luminosity, we conclude that dust mass is as good a tracer of molecular gas as CO.

(vi) At the same gas fraction, SMGs/ULIRGs have more star formation activity than 'normal' star-forming 250-μm-selected sources. This is consistent with their best-fitting SFHs which are bursty in nature.

ACKNOWLEDGEMENTS

We thank the referee for useful suggestions which improved the clarity of this paper. We thank Michal Michałowski, Malcolm Bremer, Shane Bussmann and Asantha Cooray for helpful comments. KR acknowledges support from the European Research Council Starting Grant SEDmorph (P.I. V. Wild). IRS acknowledges support from the SFTC (ST/I001573/1), a Leverhulme Trust fellowship, the ERC Advanced Grant Dustygal and a Royal Society/Wolfson Merit Award. We acknowledge the use of print-friendly colour tables by Paul Tol (http://www.sron.nl/ pault/). The *Herschel*-ATLAS is a project with *Herschel*, which is an ESA Space Observatory with science instruments provided by European-led Principal Investigator consortia and with important participation from NASA. The H-ATLAS website is http://www.h-atlas.org/. GAMA is a joint European-Australasian project based around a spectroscopic campaign using the Anglo-Australian Telescope. The GAMA input catalogue is based on data taken from the SDSS and the UKIRT Infrared Deep Sky Survey. Complementary imaging of the GAMA regions is being obtained by a number of independent survey programs including *GALEX* MIS, VST KIDS, VISTA VIKING, *WISE*, *Herschel*-ATLAS, GMRT and ASKAP providing UV to radio coverage. GAMA is funded by the STFC (UK), the ARC (Australia), the AAO and the Participating Institutions. The GAMA website is http://www.gama-survey.org/. This research has made use of data from HerMES project (http://hermes.sussex.ac.uk/). HerMES is a *Herschel* Key Programme utilizing Guaranteed Time from the SPIRE instrument team, ESAC scientists and a mission scientist. HerMES is described in Oliver et al. (2010). This research has made use of the NASA/IPAC Infrared Science Archive, which is operated by the Jet Propulsion Laboratory, California Institute of Technology, under contract with the National Aeronautics and Space Administration.

REFERENCES

Abazajian K. N. et al., 2009, ApJS, 182, 543
Adelman-McCarthy J. K. et al., 2008, ApJS, 175, 297
Alexander D. M., Bauer F. E., Chapman S. C., Smail I., Blain A. W., Brandt W. N., Ivison R. J., 2005, ApJ, 632, 736
Austermann J. E. et al., 2010, MNRAS, 401, 160
Baldry I. K. et al., 2010, MNRAS, 404, 86
Banerji M., Chapman S. C., Smail I., Alaghband-Zadeh S., Swinbank A. M., Dunlop J. S., Ivison R. J., Blain A. W., 2011, MNRAS, 418, 1071
Barger A. J., Cowie L. L., Sanders D. B., Fulton E., Taniguchi Y., Sato Y., Kawara K., Okuda H., 1998, Nature, 394, 248
Barger A. J., Cowie L. L., Wang W.-H., 2008, ApJ, 689, 687
Barnes J. E., Hernquist L. E., 1991, ApJ, 370, L65
Barnes J. E., Hernquist L., 1996, ApJ, 471, 115
Berta S. et al., 2010, A&A, 518, L30
Berta S. et al., 2011, A&A, 532, A49
Bertoldi F. et al., 2007, ApJS, 172, 132
Biggs A. D. et al., 2011, MNRAS, 413, 2314
Blain A. W., Smail I., Ivison R. J., Kneib J., Frayer D. T., 2002, Phys. Rep., 369, 111
Borys C., Scott D., Chapman S., Halpern M., Nandra K., Pope A., 2004, MNRAS, 355, 485
Bothwell M. S. et al., 2013, MNRAS, 429, 3047
Bournaud F. et al., 2011, ApJ, 730, 4
Bournaud F. et al., 2014, ApJ, 780, 57
Bourne N. et al., 2012, MNRAS, 421, 3027
Bruzual G., Charlot S., 2003, MNRAS, 344, 1000
Chabrier G., 2003, PASP, 115, 763
Chapin E. L. et al., 2009, MNRAS, 398, 1793
Chapman S. C., Blain A. W., Smail I., Ivison R. J., 2005, ApJ, 622, 772

Charlot S., Fall S. M., 2000, ApJ, 539, 718
Clements D. L., Dunne L., Eales S., 2010, MNRAS, 403, 274
Collister A. A., Lahav O., 2004, PASP, 116, 345
Combes F., García-Burillo S., Braine J., Schinnerer E., Walter F., Colina L., 2013, A&A, 550, A41
Coppin K. et al., 2010, ApJ, 713, 503
Cortese L. et al., 2012, A&A, 540, A52
da Cunha E., Charlot S., Elbaz D., 2008, MNRAS, 388, 1595 (DCE08)
da Cunha E., Eminian C., Charlot S., Blaizot J., 2010a, MNRAS, 403, 1894
da Cunha E., Charmandaris V., Díaz-Santos T., Armus L., Marshall J. A., Elbaz D., 2010b, A&A, 523, A78
Daddi E. et al., 2009, ApJ, 694, 1517
Daddi E. et al., 2010, ApJ, 714, L118
Dale D. A., Helou G., 2002, ApJ, 576, 159
Damen M. et al., 2011, ApJ, 727, 1
Dannerbauer H., Daddi E., Riechers D. A., Walter F., Carilli C. L., Dickinson M., Elbaz D., Morrison G. E., 2009, ApJ, 698, L178
Davé R., Finlator K., Oppenheimer B. D., Fardal M., Katz N., Kereš D., Weinberg D. H., 2010, MNRAS, 404, 1355
Davies J. I. et al., 2013, MNRAS, 428, 834
Dekel A. et al., 2009, Nature, 457, 451
Downes D., Solomon P. M., 1998, ApJ, 507, 615
Draine B. T. et al., 2007, ApJ, 663, 866
Driver S. P. et al., 2011, MNRAS, 413, 971
Dunne L., Eales S. A., 2001, MNRAS, 327, 697
Dunne L., Eales S., Edmunds M., Ivison R., Alexander P., Clements D. L., 2000, MNRAS, 315, 115
Dunne L., Eales S. A., Edmunds M. G., 2003, MNRAS, 341, 589
Dunne L. et al., 2011, MNRAS, 417, 1510
Dye S. et al., 2008, MNRAS, 386, 1107
Eales S., Lilly S., Gear W., Dunne L., Bond J. R., Hammer F., Le Fèvre O., Crampton D., 1999, ApJ, 515, 518
Eales S. et al., 2010a, PASP, 122, 499
Eales S. A. et al., 2010b, A&A, 518, L23
Eales S. et al., 2012, ApJ, 761, 168
Elmegreen B. G., Burkert A., 2010, ApJ, 712, 294
Engel H. et al., 2010, ApJ, 724, 233
Fazio G. G. et al., 2004, ApJS, 154, 10
Fotopoulou S. et al., 2012, ApJS, 198, 1
Gao Y., Solomon P. M., 2004, ApJ, 606, 271
Gawiser E. et al., 2006, ApJS, 162, 1
Geach J. E., Smail I., Moran S. M., MacArthur L. A., Lagos C. d. P., Edge A. C., 2011, ApJ, 730, L19
Genzel R. et al., 2008, ApJ, 687, 59
Genzel R. et al., 2010, MNRAS, 407, 2091 (G10)
Gott J. R., III, Vogeley M. S., Podariu S., Ratra B., 2001, ApJ, 549, 1
Grazian A. et al., 2006, A&A, 449, 951
Greve T. R., Ivison R. J., Bertoldi F., Stevens J. A., Dunlop J. S., Lutz D., Carilli C. L., 2004, MNRAS, 354, 779
Greve T. R. et al., 2005, MNRAS, 359, 1165
Greve T. R., Pope A., Scott D., Ivison R. J., Borys C., Conselice C. J., Bertoldi F., 2008, MNRAS, 389, 1489
Greve T. R., Papadopoulos P. P., Gao Y., Radford S. J. E., 2009, ApJ, 692, 1432
Griffin M. J. et al., 2010, A&A, 518, L3
Hainline L. J., Blain A. W., Smail I., Frayer D. T., Chapman S. C., Ivison R. J., Alexander D. M., 2009, ApJ, 699, 1610
Hainline L. J., Blain A. W., Smail I., Alexander D. M., Armus L., Chapman S. C., Ivison R. J., 2011, ApJ, 740, 96
Hao C.-N., Kennicutt R. C., Johnson B. D., Calzetti D., Dale D. A., Moustakas J., 2011, ApJ, 741, 124
Hatziminaoglou E. et al., 2010, A&A, 518, L33
Hayward C. C., Kereš D., Jonsson P., Narayanan D., Cox T. J., Hernquist L., 2011, ApJ, 743, 159
Hickox R. C. et al., 2012, MNRAS, 421, 284
Hill D. T. et al., 2011, MNRAS, 412, 765
Hodge J. A. et al., 2013, ApJ, 768, 91
Hughes D. H. et al., 1998, Nature, 394, 241
Ibar E. et al., 2010, MNRAS, 409, 38
Ilbert O. et al., 2009, ApJ, 690, 1236
Ivison R. J. et al., 2004, ApJS, 154, 124
Ivison R. J. et al., 2007, MNRAS, 380, 199
Ivison R. J., Papadopoulos P. P., Smail I., Greve T. R., Thomson A. P., Xilouris E. M., Chapman S. C., 2011, MNRAS, 412, 1913
Kennicutt R. C., Jr, 1998, ApJ, 498, 541 (K98)
Kennicutt R. C., Jr et al., 2003, PASP, 115, 928
Kennicutt R. C. et al., 2009, ApJ, 703, 1672
Kovács A., Chapman S. C., Dowell C. D., Blain A. W., Ivison R. J., Smail I., Phillips T. G., 2006, ApJ, 650, 592
Krumholz M. R., Dekel A., 2010, MNRAS, 406, 112
Lapi A. et al., 2011, ApJ, 742, 24
Lawrence A. et al., 2007, MNRAS, 379, 1599
Lee S.-K., Ferguson H. C., Somerville R. S., Wiklind T., Giavalisco M., 2010, ApJ, 725, 1644
Leroy A. K. et al., 2011, ApJ, 737, 12
Lo Faro B. et al., 2013, ApJ, 762, 108
Lutz D. et al., 2011, A&A, 532, A90
Magdis G. E. et al., 2011, ApJ, 740, L15
Magdis G. E. et al., 2012, ApJ, 760, 6
Magnelli B., Elbaz D., Chary R. R., Dickinson M., Le Borgne D., Frayer D. T., Willmer C. N. A., 2011, A&A, 528, A35
Magnelli B. et al., 2012a, A&A, 539, A155 (M12)
Magnelli B. et al., 2012b, A&A, 548, A22
Mannucci F., Cresci G., Maiolino R., Marconi A., Gnerucci A., 2010, MNRAS, 408, 2115
Maraston C., Pforr J., Renzini A., Daddi E., Dickinson M., Cimatti A., Tonini C., 2010, MNRAS, 407, 830
Marigo P., Girardi L., 2007, A&A, 469, 239
Martin D. C. et al., 2005, ApJ, 619, L1
Menéndez-Delmestre K. et al., 2009, ApJ, 699, 667
Michałowski M. J. et al., 2012a, MNRAS, 426, 1845
Michałowski M. J., Dunlop J. S., Cirasuolo M., Hjorth J., Hayward C. C., Watson D., 2012b, A&A, 541, A85
Mihos J. C., Hernquist L., 1994, ApJ, 431, L9
Mihos J. C., Hernquist L., 1996, ApJ, 464, 641
Morrissey P. et al., 2007, ApJS, 173, 682
Narayanan D., Krumholz M. R., Ostriker E. C., Hernquist L., 2012, MNRAS, 421, 3127
Netzer H. et al., 2007, ApJ, 666, 806
Nonino M. et al., 2009, ApJS, 183, 244
Oliver S. J. et al., 2010, A&A, 518, L21
Oliver S. J. et al., 2012, MNRAS, 424, 1614
Papadopoulos P. P., van der Werf P. P., Xilouris E. M., Isaak K. G., Gao Y., Mühle S., 2012, MNRAS, 426, 2601
Papovich C., Finkelstein S. L., Ferguson H. C., Lotz J. M., Giavalisco M., 2011, MNRAS, 412, 1123
Pascale E. et al., 2011, MNRAS, 415, 911
Pearson E. A. et al., 2013, MNRAS, 435, 2753
Perera T. A. et al., 2008, MNRAS, 391, 1227
Pilbratt G. L. et al., 2010, A&A, 518, L1
Poglitsch A. et al., 2010, A&A, 518, L2
Pope A. et al., 2006, MNRAS, 370, 1185
Pope A. et al., 2008, ApJ, 675, 1171
Pozzi F. et al., 2012, MNRAS, 423, 1909
Reddy N. A., Pettini M., Steidel C. C., Shapley A. E., Erb D. K., Law D. R., 2012, ApJ, 754, 25
Riechers D. A. et al., 2011, ApJ, 733, L11
Riechers D. A. et al., 2013, ApJ, preprint (arXiv:1306.5235)
Rieke G. H. et al., 2004, ApJS, 154, 25
Rigby E. E. et al., 2011, MNRAS, 415, 2336
Robotham A. et al., 2010, PASA, 27, 76
Roseboom I. G. et al., 2010, MNRAS, 409, 48
Rowlands K. et al., 2012, MNRAS, 419, 2545
Rowlands K. et al., 2014, MNRAS, preprint (arXiv:1403.2995)
Salvato M. et al., 2009, ApJ, 690, 1250
Sandstrom K. M. et al., 2013, ApJ, 777, 5

Santini P. et al., 2010, A&A, 518, L154
Scott K. S. et al., 2008, MNRAS, 385, 2225
Scott K. S. et al., 2010, MNRAS, 405, 2260
Scoville N., 2013, in Wong T., Ott J., eds, Proc. IAU Symp. 292, Evolution of ISM Contents of Massive Galaxies from z = 2 to 0.3. Cambridge Univ. Press, Cambridge, p. 279
Seaquist E., Yao L., Dunne L., Cameron H., 2004, MNRAS, 349, 1428
Simpson J. et al., 2014, ApJ, preprint (arXiv:1310.6363)
Smail I., Ivison R. J., Blain A. W., 1997, ApJ, 490, L5
Smith D. J. B. et al., 2011, MNRAS, 416, 857
Smith A. J. et al., 2012a, MNRAS, 419, 377
Smith D. J. B. et al., 2012b, MNRAS, 427, 703
Smith M. W. L. et al., 2012c, ApJ, 748, 123
Smith D. J. B. et al., 2013, MNRAS, 436, 2435
Sobral D., Smail I., Best P. N., Geach J. E., Matsuda Y., Stott J. P., Cirasuolo M., Kurk J., 2013, MNRAS, 428, 1128
Solomon P. M., Downes D., Radford S. J. E., Barrett J. W., 1997, ApJ, 478, 144
Stott J. P. et al., 2013, MNRAS, 436, 1130
Sutherland W., Saunders W., 1992, MNRAS, 259, 413
Swinbank A. M., Chapman S. C., Smail I., Lindner C., Borys C., Blain A. W., Ivison R. J., Lewis G. F., 2006, MNRAS, 371, 465
Swinbank A. M. et al., 2011, ApJ, 742, 11
Swinbank A. M. et al., 2014, MNRAS, 438, 1267
Symeonidis M. et al., 2013, MNRAS, 431, 2317
Tacconi L. J. et al., 2006, ApJ, 640, 228
Tacconi L. J. et al., 2008, ApJ, 680, 246
Tacconi L. J. et al., 2013, ApJ, 768, 74
Targett T. A. et al., 2013, MNRAS, 432, 2012
Taylor E. N. et al., 2009, ApJS, 183, 295
van de Voort F., Schaye J., Booth C. M., Haas M. R., Dalla Vecchia C., 2011, MNRAS, 414, 2458
Wang W.-H., Cowie L. L., Barger A. J., Keenan R. C., Ting H.-C., 2010, ApJS, 187, 251
Wang W.-H., Cowie L. L., Barger A. J., Williams J. P., 2011, ApJ, 726, L18
Wardlow J. L. et al., 2011, MNRAS, 415, 1479
Yao L., Seaquist E. R., Kuno N., Dunne L., 2003, ApJ, 588, 771
Younger J. D. et al., 2007, ApJ, 671, 1531
Younger J. D. et al., 2009, ApJ, 704, 803
Yun M. S. et al., 2012, MNRAS, 420, 957

APPENDIX A: STANDARD AND SMG PRIORS

Here, we highlight the parameters which are different in the standard and SMG prior libraries. A summary of standard and SMG prior distributions are shown in Fig. A1.

Optical depth: from DCE08, the standard priors for $\hat{\tau}_V$ and $\hat{\tau}_V^{\rm ISM}$, the total effective *V*-band optical depth seen by stars in birth clouds and in the ambient ISM, respectively, range from 0 to 6. This describes the full range of attenuations observed for normal low-redshift galaxies (DCE08, and references within). When fitting the SEDs of SMGs with the standard priors, the $\hat{\tau}_V$ PDF frequently runs up against the upper edge of the prior space. This suggests that the $\hat{\tau}_V$ prior in the standard libraries does not extend to sufficiently high values to fully describe the properties of SMGs (which are known to be more obscured than local galaxies; Menéndez-Delmestre et al. 2009). As with the ULIRG priors in da Cunha et al. (2010b), the $\hat{\tau}_V$ and $\hat{\tau}_V^{\rm ISM}$priors are modified to allow for higher optical depths so that they now range between 0 and 20.

Star formation history (SFH): the standard prior for the SFH is parametrized as an exponentially decreasing model of the form $\exp(-\gamma t)$, where γ is the star formation time-scale parameter and is distributed uniformly between 0 and 1 Gyr^{-1}. For SMGs, we adopt both exponentially increasing and decreasing SFRs by distributing the γ parameter as a Gaussian between -1 and 1 Gyr^{-1}, as many studies (Lee et al. 2010; Maraston et al. 2010; Papovich et al. 2011; Reddy et al. 2012) found that an exponentially increasing SFR may be appropriate for some high-redshift galaxies.

Bursts are superimposed at random times on the continuous SFH, but with a probability that 50 per cent of galaxies experience a burst in the last 2 Gyr. The strength of the burst is defined as the mass of stars formed in the burst relative to the mass of stars formed in continuous star formation over the lifetime of the galaxy. This parameter ranges from 0.03 to 4.0 with logarithmic spacing in the standard prior. Since SMGs are thought to be experiencing strong starbursts, the burst strength is increased to range from 0.1 to 100.

The time since the start of star formation in the galaxy ($t_{\rm form}$) is uniformly distributed between 0.1 and 13.5 Gyr in the standard prior. The lower limit is decreased from 0.1 to 0.01 Gyr in the SMG prior in order to increase both the number of models with SSFR $\sim 1 \times 10^{-8}$ yr^{-1} and to extend the upper limit of the SSFR prior from $\sim 1 \times 10^{-8}$ to $\sim 1 \times 10^{-7}$ yr^{-1}.

Birth cloud time-scale: moderately star-forming galaxies in the local Universe are assumed in the DCE08 model to have a fixed birth cloud time-scale ($t_{\rm BC}$) of 1×10^7 yr, after which the young stars move from their birth clouds into the less obscured diffuse ISM. da Cunha et al. (2010b) found that $t_{\rm BC} = 1 \times 10^8$ yr was more appropriate for ULIRGs, which are more heavily obscured than normal star-forming galaxies. For the SMGs, we allowed $t_{\rm BC}$ to vary as a free parameter which is uniformly distributed in logarithmic space between 1×10^7 and 1×10^8 yr. This accounts for the possibility of longer birth cloud lifetimes in gas-rich discs (Krumholz & Dekel 2010) but does not force SMGs to have such extreme opacities as local ULIRGs.

Dust temperatures: the temperature of the cold dust component is extended from 15−25 K to 15−30 K, as was done for the ULIRGs in da Cunha et al. (2010b). The greater intensity of star formation in the SMGs could produce higher ambient dust temperatures in the ISM, due to an increase in the hardness of the interstellar radiation field.

A1 Comparison of priors

Fig. A2 shows the parameter values derived using the standard MAGPHYS and SMG libraries for the 29 high-redshift SMGs with good SED fits (of which four are AGN power-law subtracted SEDs). The parameters which appear to be most sensitive to the choice of prior are f_μ , $\hat{\tau}_V$ and SSFR, which is not unexpected given this was the aim of altering the priors. Increasing $\hat{\tau}_V$ and the birth cloud time-scale in the SMG priors results in more of the dust luminosity (which is constrained very well by observations) being produced in the birth clouds in the model. Around 50 per cent of our sources have SSFRs significantly higher than that would be obtained using the standard priors. Parameters where we did not specifically alter the prior (e.g. $M_{\rm d}$, SFR, M_*) are reassuringly not very different. There is a slight tendency for stellar masses and dust masses to be lower with the SMG priors, this is a systematic change but still within the median error range for these parameters. In the majority of cases, the choice of prior for the SMGs does not change our conclusions in Section 4. Where the choice of prior influences our results, we highlight the effect when interpreting our findings.

APPENDIX B: SED FITS

We present the panchromatic SED fits for the sample of SMGs studied in this paper, using the MAGPHYS SMG priors described in Section 3.

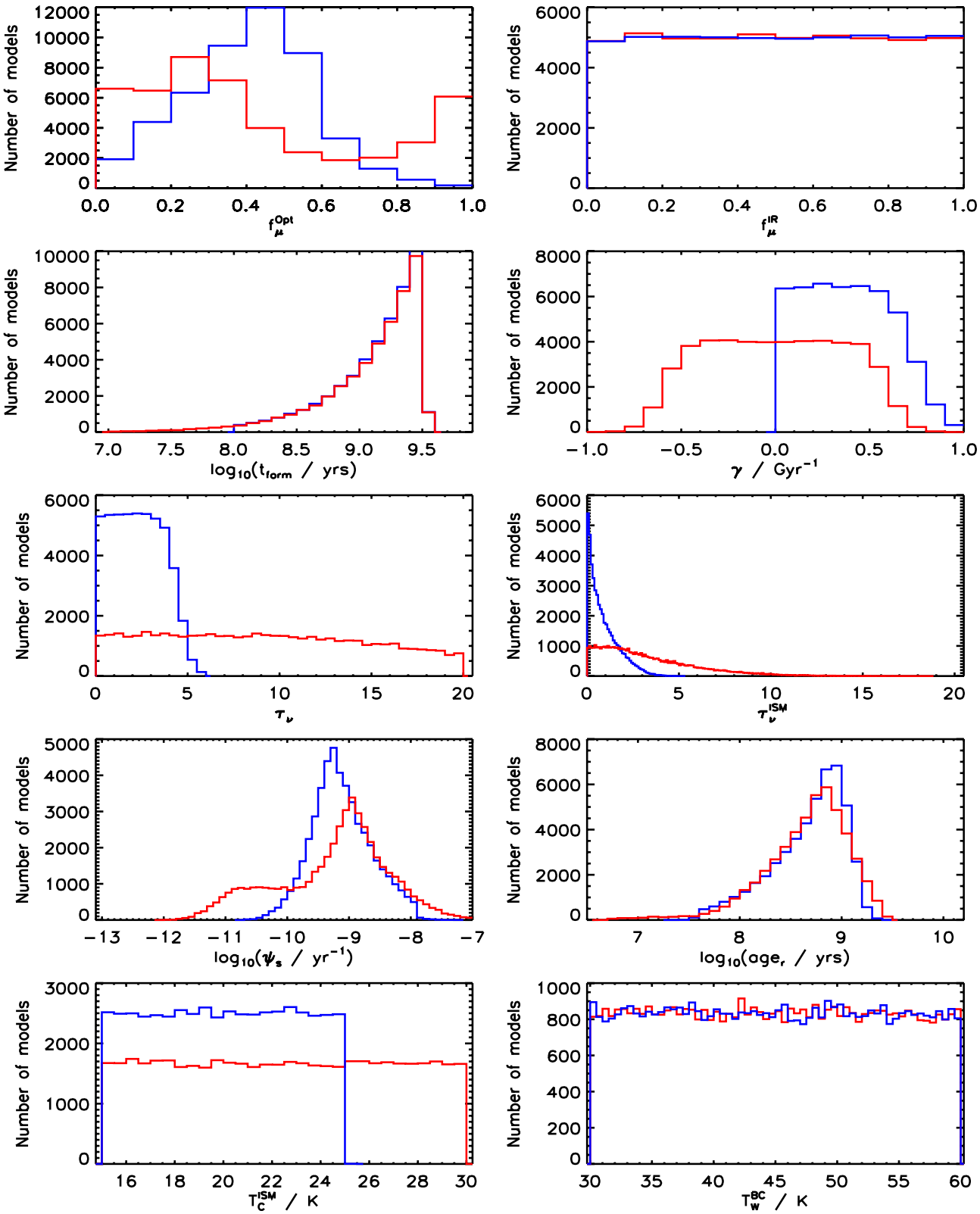

Figure A1. Comparison of the standard (blue histogram) and SMG (red histogram) prior distributions for parameters relevant to this work at $z \sim 2$. The panels are: $f_\mu^{\rm Opt}$, the fraction of total dust luminosity contributed by the diffuse ISM in the optical model; $f_\mu^{\rm IR}$, the fraction of total dust luminosity contributed by the diffuse ISM in the infrared model; γ, the star formation time-scale (Gyr^{-1}); $\hat{\tau}_V$, total effective V-band optical depth seen by stars in birth clouds; $\hat{\tau}_V^{\rm ISM}$, the total effective V-band optical depth in the ambient ISM; $\psi_{\rm S}$/ yr^{-1}, SSFR, age$_r$, r-band light-weighted age; $T_{\rm C}^{\rm ISM}$/K, temperature of the cold diffuse ISM dust component; and $T_{\rm W}^{\rm BC}$/K, temperature of the warm dust component in birth clouds.

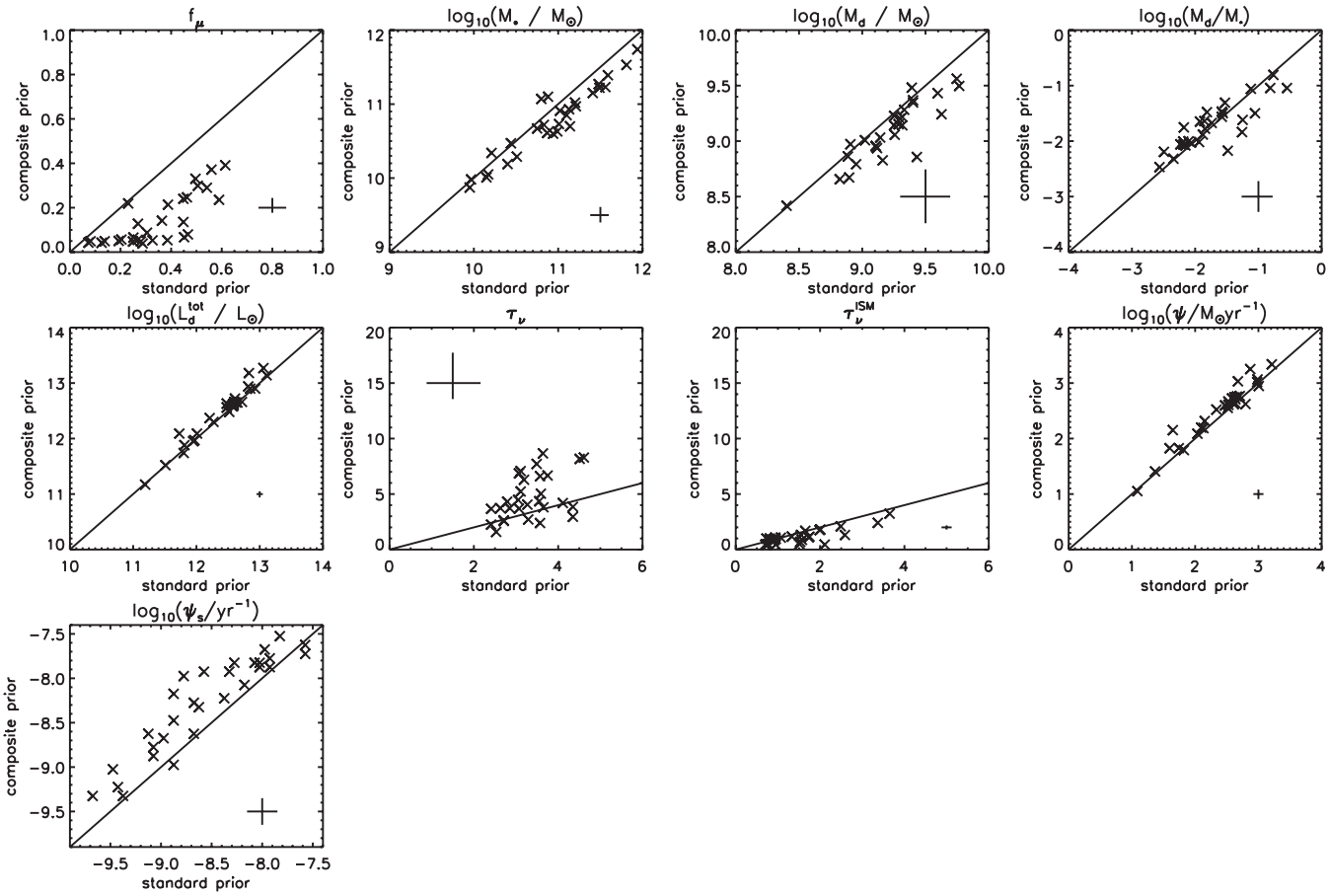

Figure A2. A comparison of median-likelihood values of different parameters using the standard MAGPHYS prior libraries and the new SMG priors for the 29 SMGs in Section 4. Note that where the axis ranges are different, these reflect the width of the priors. Solid black lines show the one-to-one line for each parameter. The error bar indicates the median 84th–16th percentile range from the parameter PDF. The parameters shown are: f_μ, the fraction of total dust luminosity contributed by the diffuse ISM; $M_*/\mathrm{M}_\odot$, stellar mass; $M_\mathrm{d}/\mathrm{M}_\odot$, dust mass; M_d/M_* , dust-to-stellar mass ratio; $L_\mathrm{d}/\mathrm{L}_\odot$, dust luminosity; $\hat{\tau}_V$, total effective V-band optical depth seen by stars in birth clouds; $\hat{\tau}_V^{\mathrm{ISM}}$, the total effective V-band optical depth in the ambient ISM; $\psi/\mathrm{M}_\odot\ \mathrm{yr}^{-1}$, the SFR; and $\psi_\mathrm{S}/\mathrm{yr}^{-1}$, the SSFR averaged over the last 10^7 yr.

APPENDIX C: AGN

Some SMGs in our sample show excess emission in the rest-frame NIR, which may be due to dust heated to high temperatures by an obscured AGN (Hainline et al. 2011). The MAGPHYS SED models do not include a prescription for AGN emission and so we must assess the impact that AGN emission may have on the parameters.

To select galaxies from our SMG sample which have power-law emission in the NIR, we use the $S_{24}/S_{8.0}-S_{8.0}/S_{4.5}$ diagram from Ivison et al. (2004) and the colour cut $S_{8.0}/S_{4.5} > 1.65$ from Coppin et al. (2010). We find that 6/34 galaxies at $z > 1$ are classified as AGN (AzLOCK.01, AzLOCK.10, AzTECJ100019+023206, GN20, LOCK850.04 and LOCK850.15). We note that our sample may be slightly biased towards AGN because of the requirement of strong emission lines in order to measure a spectroscopic redshift.

We quantify the effect of power-law emission on the derived physical parameters of SMGs selected to have a NIR excess. Following the method in Hainline et al. (2011), we parametrize the NIR excess emission as a simple power law with $f_\lambda \propto \lambda^\alpha$. The power-law parametrization does not include any prescription for dust extinction. We use values of $\alpha = 2$ and 3 which are appropriate for SMGs (Hainline et al. 2011, and references within). We normalize the power law to the observed 8 μm data point which is the maximum power-law fraction. We then subtract from all photometry shortwards of 8 μm the power-law flux in increments of 0.1 times the maximum power-law fraction. We fit the power-law subtracted SED at each increment to determine the galaxy physical parameters. The power-law contribution to each galaxy SED is determined as the combination of power law and stellar emission model from MAGPHYS which results in the best-fitting SED. Examples of the power-law subtraction method are shown in Fig. B1. When the power-law

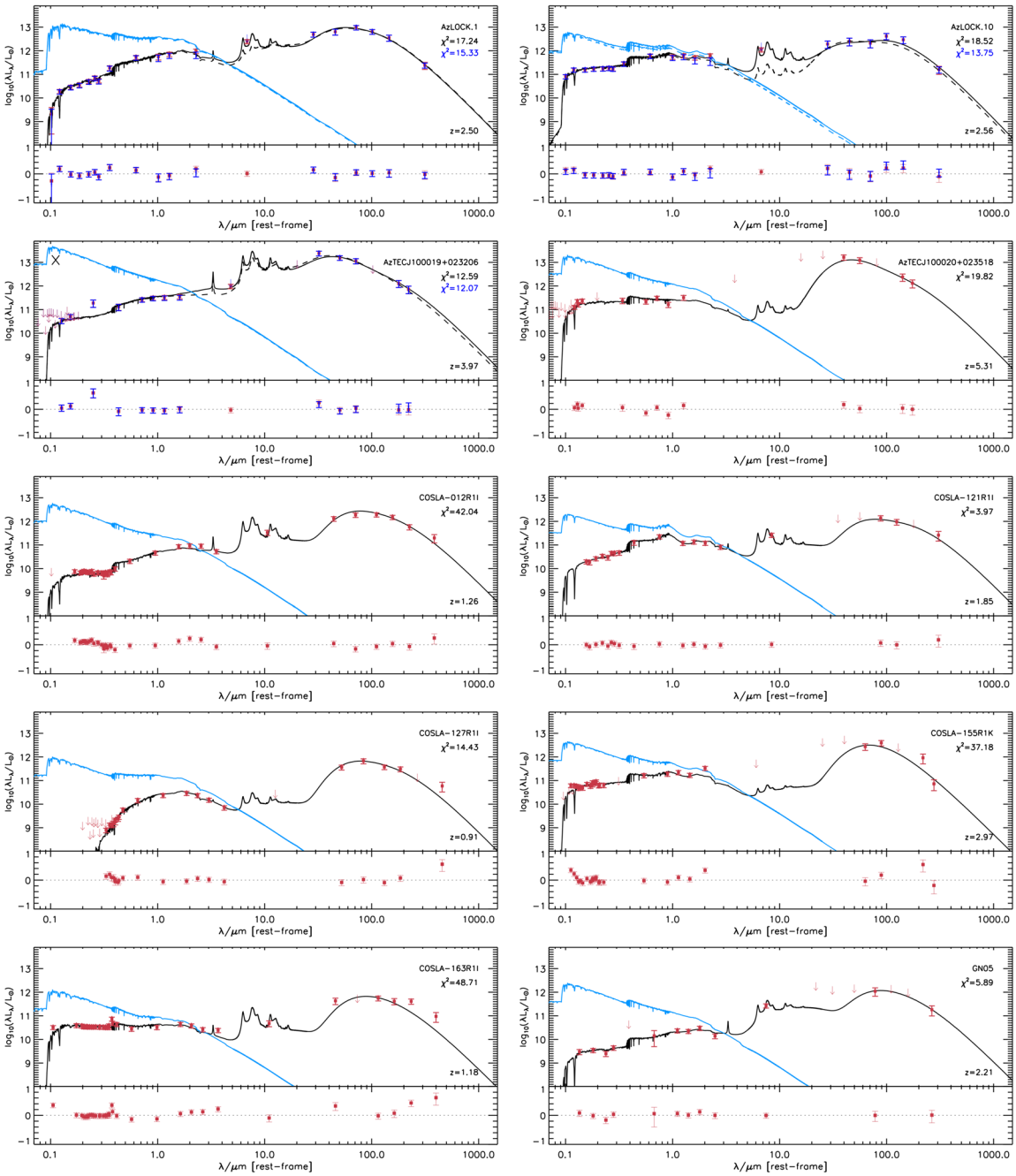

Figure B1. Multiwavelength SEDs of the 34 SMGs in our sample (including five rejected fits indicated by a black cross in the top-left corner of each plot), with observed photometry (red points) from the rest-frame UV to the submillimetre. Upper limits are shown as arrows, and errors on the photometry are described in Section 2.2. The solid black line is the best-fitting model SED and the solid blue line is the unattenuated optical model. The residuals of the fit are shown in the panel below each SED. In the case where we have subtracted a power-law component to account for hot dust emission from an AGN, the dashed lines indicate the best-fitting model and the blue points indicate the power-law subtracted photometry.

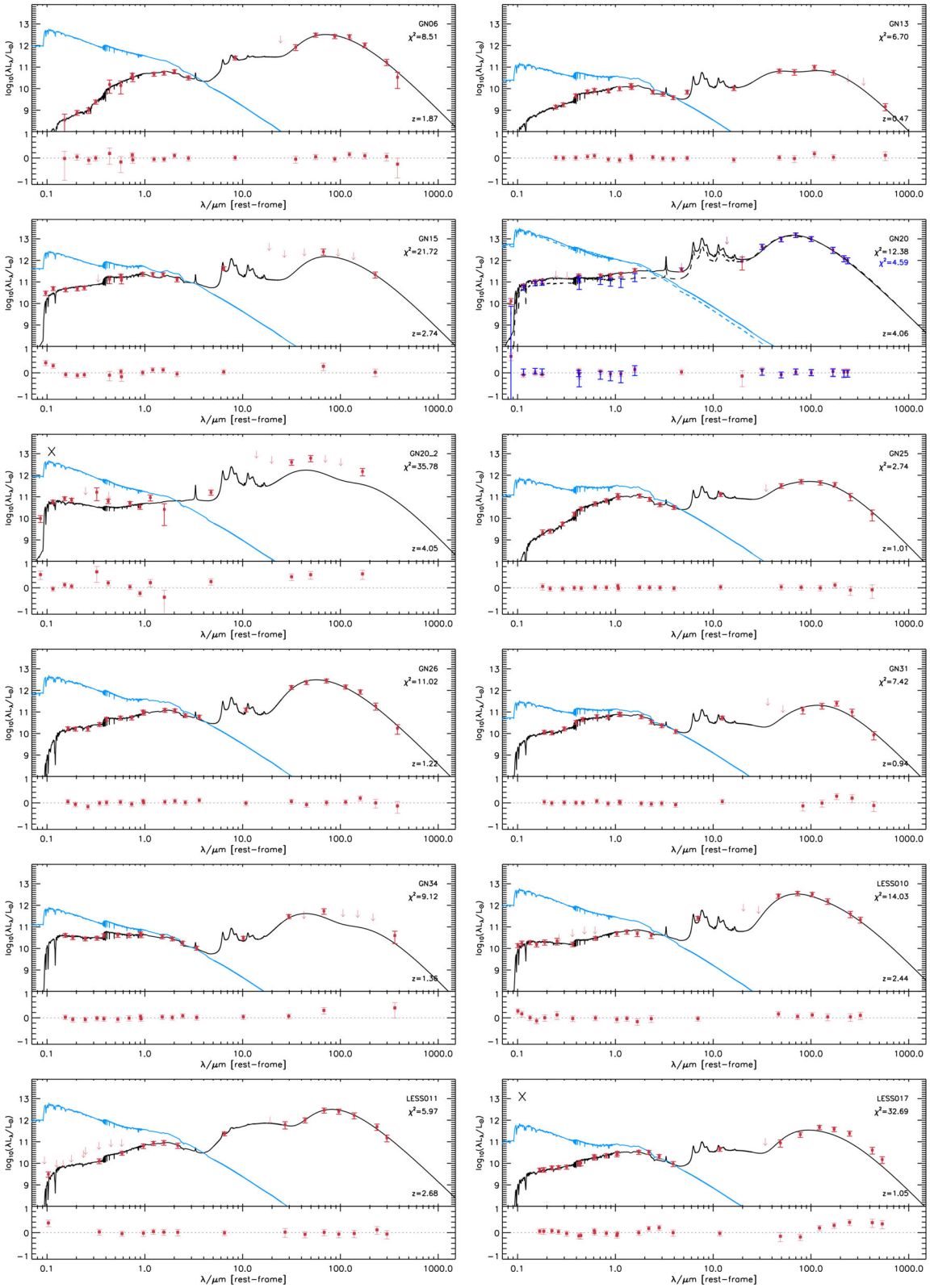

Figure B1 – *continued*

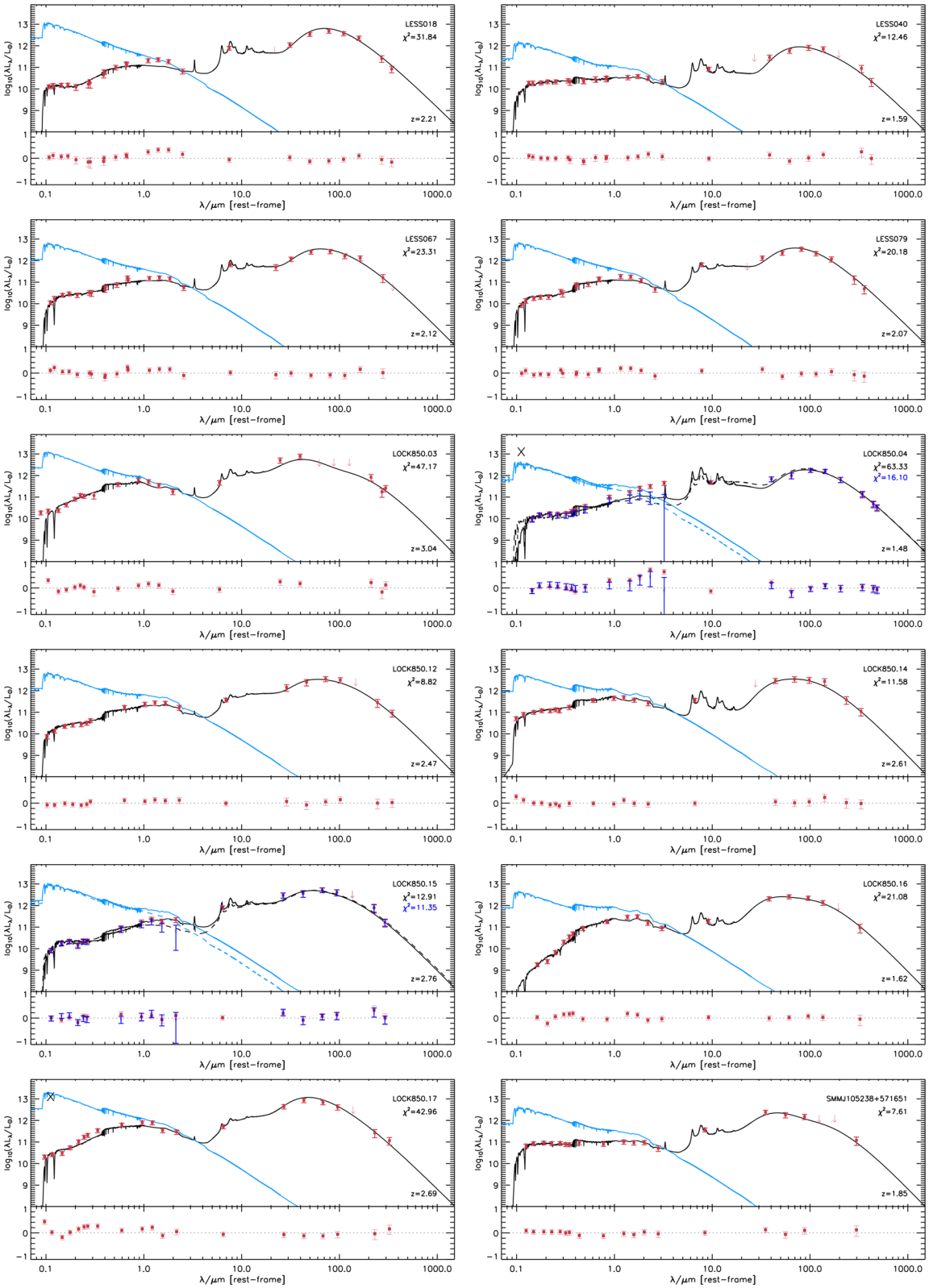

Figure B1 – *continued*

Table D1. Properties of the 29 SMGs (those with good SED fits) derived from SED fitting. The columns are (from left to right): Name, redshift, f_μ, the fraction of total dust luminosity contributed by the diffuse ISM; $M_*/\mathrm{M}_\odot$, stellar mass; $M_\mathrm{d}/\mathrm{M}_\odot$, dust mass; M_d/M_* , dust to stellar mass ratio; $L_\mathrm{d}/\mathrm{L}_\odot$, dust luminosity; $\hat{\tau}_V$, total effective V-band optical depth seen by stars in birth clouds; $\hat{\tau}_V^\mathrm{ISM}$, the total effective V-band optical depth in the ambient ISM $\psi/\mathrm{M}_\odot\ \mathrm{yr}^{-1}$, the SFR averaged over the last 10^7 yr and $\psi_\mathrm{S}/\mathrm{yr}^{-1}$, the SSFR averaged over the last 10^7 yr. Uncertainties are indicated by the median 84th–16th percentile range from each individual parameter PDF. Parameters derived from an AGN power-law subtracted SED are denoted with a †.

Name	z	f_μ	M_*	M_d	M_d/M_*	L_d	$\hat{\tau}_V$	$\hat{\tau}_V^\mathrm{ISM}$	ψ	ψ_S
AzLOCK.1†	2.50	$0.24^{+0.07}_{-0.09}$	$11.74^{+0.13}_{-0.10}$	$9.43^{+0.18}_{-0.17}$	$-2.32^{+0.22}_{-0.20}$	$13.14^{+0.05}_{-0.05}$	$6.67^{+5.38}_{-2.80}$	$1.75^{+0.22}_{-0.26}$	$3.07^{+0.08}_{-0.08}$	$-8.68^{+0.15}_{-0.20}$
AzLOCK.10†	2.56	$0.25^{+0.06}_{-0.07}$	$11.39^{+0.06}_{-0.08}$	$9.37^{+0.25}_{-0.25}$	$-2.01^{+0.26}_{-0.28}$	$12.65^{+0.07}_{-0.07}$	$3.73^{+3.52}_{-1.44}$	$0.85^{+0.08}_{-0.16}$	$2.61^{+0.08}_{-0.08}$	$-8.77^{+0.15}_{-0.15}$
AzTECJ100020+023518	5.31	$0.04^{+0.03}_{-0.02}$	$11.10^{+0.06}_{-0.10}$	$9.24^{+0.52}_{-0.30}$	$-1.84^{+0.52}_{-0.33}$	$13.18^{+0.11}_{-0.10}$	$7.07^{+0.76}_{-3.12}$	$0.83^{+0.12}_{-0.18}$	$3.25^{+0.11}_{-0.08}$	$-7.88^{+0.10}_{-0.01}$
COSLA-012R1I	1.26	$0.06^{+0.02}_{-0.02}$	$10.29^{+0.01}_{-0.01}$	$9.50^{+0.28}_{-0.24}$	$-0.81^{+0.26}_{-0.24}$	$12.61^{+0.01}_{-0.01}$	$3.85^{+0.01}_{-0.01}$	$0.45^{+0.01}_{-0.01}$	$2.77^{+0.01}_{-0.01}$	$-7.53^{+0.01}_{-0.01}$
COSLA-121R1I	1.85	$0.30^{+0.07}_{-0.09}$	$11.02^{+0.16}_{-0.10}$	$9.14^{+0.48}_{-0.38}$	$-1.88^{+0.49}_{-0.40}$	$12.30^{+0.05}_{-0.09}$	$3.73^{+4.76}_{-1.38}$	$1.17^{+0.14}_{-0.14}$	$2.19^{+0.09}_{-0.10}$	$-8.88^{+0.20}_{-0.15}$
COSLA-127R1I	0.91	$0.24^{+0.21}_{-0.11}$	$10.91^{+0.27}_{-0.24}$	$8.86^{+0.38}_{-0.28}$	$-2.03^{+0.38}_{-0.40}$	$11.88^{+0.06}_{-0.07}$	$8.17^{+4.58}_{-0.92}$	$2.41^{+1.02}_{-0.20}$	$1.83^{+0.12}_{-0.20}$	$-9.23^{+0.45}_{-0.15}$
COSLA-155R1K	2.97	$0.13^{+0.08}_{-0.07}$	$10.85^{+0.11}_{-0.04}$	$8.79^{+0.22}_{-0.22}$	$-2.08^{+0.24}_{-0.24}$	$12.56^{+0.15}_{-0.23}$	$4.47^{+2.74}_{-2.10}$	$0.93^{+0.12}_{-0.24}$	$2.55^{+0.17}_{-0.25}$	$-8.27^{+0.15}_{-0.35}$
COSLA-163R1I	1.18	$0.06^{+0.02}_{-0.03}$	$9.87^{+0.16}_{-0.01}$	$8.86^{+0.26}_{-0.24}$	$-1.04^{+0.26}_{-0.24}$	$11.95^{+0.01}_{-0.01}$	$2.25^{+2.18}_{-0.01}$	$0.41^{+0.16}_{-0.01}$	$2.09^{+0.01}_{-0.09}$	$-7.78^{+0.01}_{-0.15}$
GN05	2.21	$0.07^{+0.07}_{-0.05}$	$10.19^{+0.11}_{-0.24}$	$8.66^{+0.41}_{-0.49}$	$-1.50^{+0.40}_{-0.51}$	$12.09^{+0.18}_{-0.17}$	$5.03^{+3.38}_{-1.88}$	$1.17^{+0.46}_{-0.42}$	$2.15^{+0.17}_{-0.21}$	$-7.97^{+0.25}_{-0.30}$
GN06	1.87	$0.14^{+0.07}_{-0.10}$	$10.93^{+0.12}_{-0.14}$	$9.15^{+0.16}_{-0.15}$	$-1.78^{+0.20}_{-0.20}$	$12.62^{+0.03}_{-0.04}$	$8.29^{+5.36}_{-3.46}$	$3.23^{+0.32}_{-1.56}$	$2.60^{+0.08}_{-0.07}$	$-8.32^{+0.20}_{-0.15}$
GN13	0.48	$0.33^{+0.29}_{-0.07}$	$9.98^{+0.04}_{-0.07}$	$8.42^{+0.23}_{-0.31}$	$-1.56^{+0.25}_{-0.32}$	$11.17^{+0.04}_{-0.03}$	$6.87^{+7.04}_{-2.64}$	$1.69^{+0.46}_{-0.26}$	$1.05^{+0.11}_{-2.32}$	$-8.98^{+0.20}_{-2.24}$
GN15	2.74	$0.21^{+0.08}_{-0.08}$	$10.97^{+0.10}_{-0.10}$	$8.95^{+0.35}_{-0.31}$	$-2.00^{+0.35}_{-0.34}$	$12.37^{+0.13}_{-0.18}$	$3.69^{+2.78}_{-1.28}$	$0.99^{+0.20}_{-0.18}$	$2.32^{+0.19}_{-0.18}$	$-8.62^{+0.20}_{-0.30}$
GN20†	4.06	$0.04^{+0.02}_{-0.03}$	$11.07^{+0.04}_{-0.04}$	$9.56^{+0.22}_{-0.13}$	$-1.50^{+0.30}_{-0.16}$	$13.27^{+0.02}_{-0.03}$	$8.66^{+0.01}_{-1.88}$	$1.09^{+0.15}_{-0.38}$	$3.34^{+0.05}_{-0.02}$	$-7.72^{+0.01}_{-0.01}$
GN25	1.01	$0.39^{+0.09}_{-0.09}$	$11.15^{+0.13}_{-0.11}$	$8.97^{+0.23}_{-0.25}$	$-2.19^{+0.26}_{-0.27}$	$11.97^{+0.03}_{-0.05}$	$6.61^{+5.20}_{-2.44}$	$1.81^{+0.18}_{-0.18}$	$1.83^{+0.06}_{-0.08}$	$-9.32^{+0.15}_{-0.20}$
GN26	1.22	$0.07^{+0.05}_{-0.04}$	$10.72^{+0.09}_{-0.20}$	$8.67^{+0.19}_{-0.13}$	$-2.02^{+0.23}_{-0.18}$	$12.58^{+0.03}_{-0.03}$	$4.35^{+2.36}_{-1.06}$	$1.09^{+0.18}_{-0.56}$	$2.64^{+0.05}_{-0.04}$	$-8.07^{+0.25}_{-0.15}$
GN31	0.94	$0.37^{+0.48}_{-0.10}$	$10.67^{+0.13}_{-0.12}$	$9.01^{+0.16}_{-0.22}$	$-1.67^{+0.22}_{-0.24}$	$11.52^{+0.06}_{-0.06}$	$3.67^{+2.86}_{-1.72}$	$0.89^{+0.38}_{-0.20}$	$1.41^{+0.12}_{-1.63}$	$-9.32^{+0.25}_{-1.70}$
GN34	1.36	$0.09^{+0.05}_{-0.05}$	$10.05^{+0.09}_{-0.07}$	$7.89^{+0.68}_{-0.43}$	$-2.17^{+0.69}_{-0.44}$	$11.74^{+0.05}_{-0.07}$	$2.63^{+1.36}_{-1.18}$	$0.47^{+0.16}_{-0.18}$	$1.79^{+0.08}_{-0.07}$	$-8.23^{+0.10}_{-0.20}$
LESS010	2.44	$0.05^{+0.02}_{-0.03}$	$10.34^{+0.22}_{-0.01}$	$9.35^{+0.29}_{-0.20}$	$-1.04^{+0.31}_{-0.24}$	$12.63^{+0.10}_{-0.01}$	$3.81^{+0.68}_{-0.01}$	$0.45^{+0.34}_{-0.01}$	$2.74^{+0.07}_{-0.01}$	$-7.62^{+0.01}_{-0.15}$
LESS011	2.68	$0.05^{+0.11}_{-0.04}$	$10.61^{+0.34}_{-0.25}$	$9.28^{+0.14}_{-0.13}$	$-1.31^{+0.28}_{-0.40}$	$12.59^{+0.05}_{-0.04}$	$4.19^{+5.64}_{-1.04}$	$1.31^{+1.24}_{-0.94}$	$2.67^{+0.07}_{-0.12}$	$-7.93^{+0.25}_{-0.45}$
LESS018	2.21	$0.04^{+0.03}_{-0.03}$	$10.73^{+0.43}_{-0.34}$	$9.23^{+0.11}_{-0.11}$	$-1.48^{+0.35}_{-0.36}$	$12.90^{+0.01}_{-0.08}$	$2.39^{+2.12}_{-0.22}$	$0.41^{+0.50}_{-0.10}$	$3.02^{+0.06}_{-0.12}$	$-7.82^{+0.50}_{-0.30}$
LESS040	1.59	$0.05^{+0.02}_{-0.02}$	$10.01^{+0.01}_{-0.02}$	$8.94^{+0.23}_{-0.18}$	$-1.06^{+0.23}_{-0.19}$	$12.09^{+0.08}_{-0.01}$	$5.23^{+0.01}_{-2.20}$	$0.95^{+0.01}_{-0.44}$	$2.20^{+0.10}_{-0.01}$	$-7.82^{+0.10}_{-0.01}$
LESS067	2.12	$0.05^{+0.05}_{-0.03}$	$10.60^{+0.51}_{-0.23}$	$8.96^{+0.24}_{-0.19}$	$-1.64^{+0.30}_{-0.35}$	$12.65^{+0.06}_{-0.05}$	$2.71^{+3.58}_{-0.56}$	$0.69^{+0.28}_{-0.22}$	$2.76^{+0.04}_{-0.05}$	$-7.82^{+0.20}_{-0.55}$
LESS079	2.07	$0.05^{+0.04}_{-0.04}$	$10.70^{+0.17}_{-0.23}$	$9.03^{+0.17}_{-0.14}$	$-1.65^{+0.25}_{-0.27}$	$12.66^{+0.05}_{-0.04}$	$2.57^{+1.06}_{-0.72}$	$0.87^{+0.10}_{-0.40}$	$2.72^{+0.06}_{-0.02}$	$-7.93^{+0.15}_{-0.25}$
LOCK850.03	3.04	$0.08^{+0.03}_{-0.02}$	$11.23^{+0.01}_{-0.02}$	$9.48^{+0.24}_{-0.26}$	$-1.75^{+0.28}_{-0.30}$	$12.94^{+0.01}_{-0.03}$	$1.59^{+0.32}_{-0.01}$	$0.49^{+0.80}_{-0.01}$	$3.03^{+0.01}_{-0.09}$	$-8.18^{+0.01}_{-0.05}$
LOCK850.12	2.47	$0.14^{+0.09}_{-0.09}$	$11.22^{+0.11}_{-0.14}$	$9.14^{+0.26}_{-0.22}$	$-2.06^{+0.28}_{-0.26}$	$12.72^{+0.03}_{-0.10}$	$6.29^{+2.64}_{-2.04}$	$1.31^{+0.14}_{-0.34}$	$2.71^{+0.14}_{-0.13}$	$-8.48^{+0.10}_{-0.15}$
LOCK850.14	2.61	$0.22^{+0.08}_{-0.07}$	$11.27^{+0.07}_{-0.08}$	$9.20^{+0.24}_{-0.21}$	$-2.06^{+0.25}_{-0.24}$	$12.66^{+0.07}_{-0.08}$	$4.05^{+3.62}_{-1.60}$	$0.99^{+0.18}_{-0.14}$	$2.62^{+0.08}_{-0.09}$	$-8.62^{+0.10}_{-0.15}$
LOCK850.15†	2.76	$0.05^{+0.03}_{-0.03}$	$10.63^{+0.22}_{-0.02}$	$9.22^{+0.33}_{-0.30}$	$-1.47^{+0.36}_{-0.33}$	$12.90^{+0.02}_{-0.10}$	$2.95^{+2.04}_{-0.18}$	$1.07^{+0.22}_{-0.70}$	$2.95^{+0.08}_{-0.09}$	$-7.68^{+0.01}_{-0.30}$
LOCK850.16	1.62	$0.29^{+0.09}_{-0.13}$	$11.53^{+0.06}_{-0.11}$	$9.06^{+0.31}_{-0.26}$	$-2.47^{+0.33}_{-0.28}$	$12.60^{+0.05}_{-0.05}$	$7.71^{+4.36}_{-4.34}$	$2.09^{+0.18}_{-0.64}$	$2.52^{+0.07}_{-0.12}$	$-9.02^{+0.20}_{-0.15}$
SMMJ105238+571651	1.85	$0.05^{+0.02}_{-0.03}$	$10.47^{+0.18}_{-0.33}$	$8.83^{+0.54}_{-0.54}$	$-1.62^{+0.54}_{-0.56}$	$12.48^{+0.05}_{-0.01}$	$4.31^{+0.24}_{-2.52}$	$0.51^{+0.28}_{-0.16}$	$2.62^{+0.04}_{-0.05}$	$-7.88^{+0.40}_{-0.15}$

fraction is large, the optical emission can be oversubtracted; in this case, we set the flux density to an upper limit at the value of the power law. There is evidence to suggest that the power-law slope in the MIR is different to that in the optical–NIR, and Hainline et al. (2011) found that extrapolation of the NIR power law longwards of 8 μm does not give a good prediction of the 24 μm flux density. Given the uncertainty in the AGN contribution to the MIR emission, we include data with $5 < \lambda_\mathrm{rest} < 30$ μm as an upper limit in the SED fitting procedure. We assume that photometry longwards of rest-frame 30 μm has a negligible contribution from AGN emission (Netzer et al. 2007; Hatziminaoglou et al. 2010; Pozzi et al. 2012).

APPENDIX D: PHYSICAL PROPERTIES OF SMGS

In Table D1, we show the median-likelihood physical parameters for each individual SMG derived from the MAGPHYS SED fitting, as described in Section 3.

APPENDIX E: MAGPHYS STAR FORMATION HISTORIES

The SFHs derived from our SED fitting in Section 4 are shown in Fig. E1.

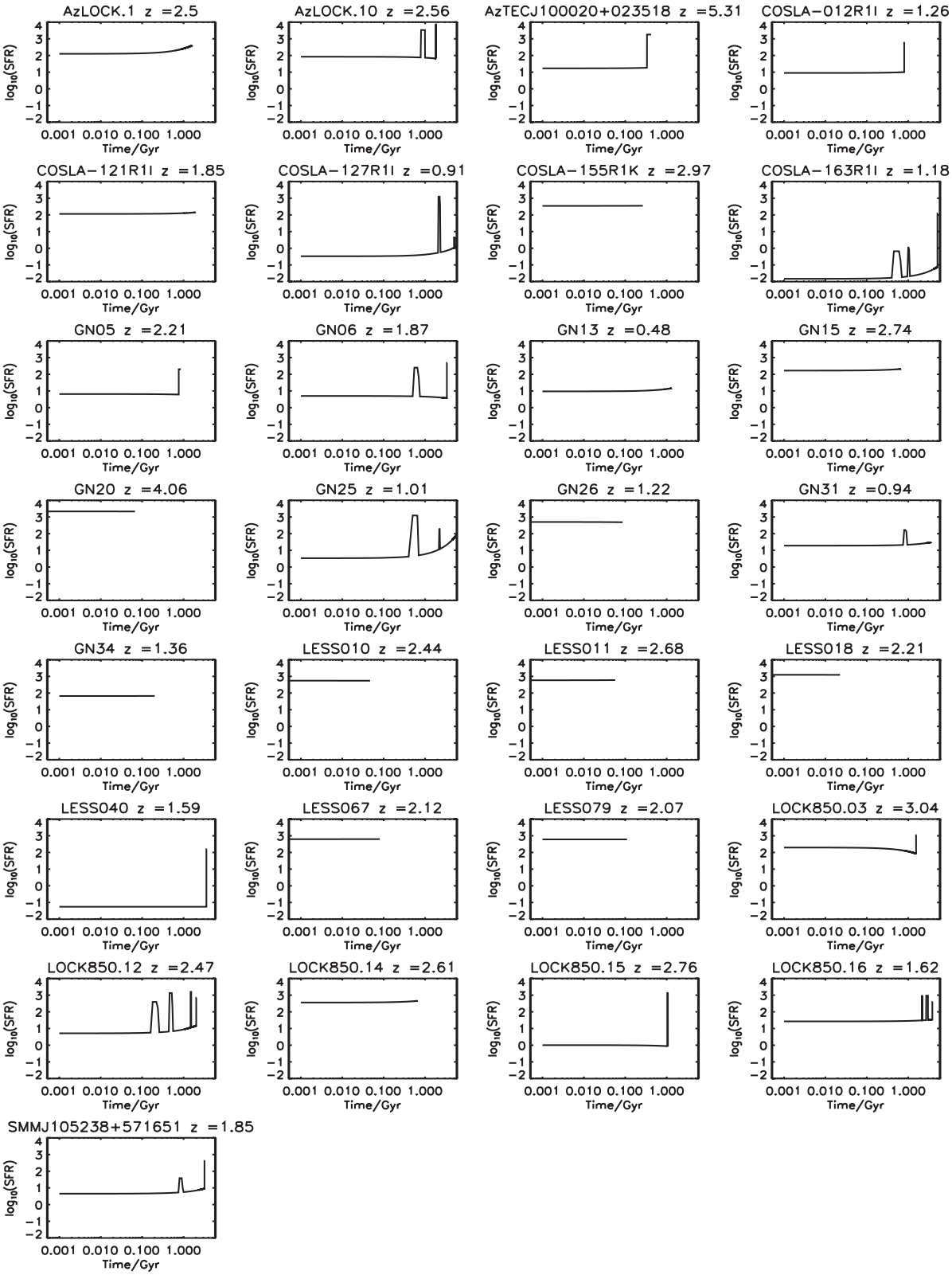

Figure E1. Best-fitting SFHs of the 29 SMGs with good SED fits derived from MAGPHYS SED fitting. The majority of SFHs can be described as 'bursts' of star formation, either because they have a short elevated SFR near the current age or because their SFHs are so short and extreme that they can be considered a burst.

This paper has been typeset from a TEX/LATEX file prepared by the author.